

Revealing stellar brightness profiles by means of microlensing fold caustics

M. Dominik

University of St Andrews, School of Physics & Astronomy, North Haugh, St Andrews, KY16 9SS

2 February 2008

ABSTRACT

With a handful of measurements of limb-darkening coefficients, galactic microlensing has already proven to be a powerful technique for studying atmospheres of distant stars. Survey campaigns such as OGLE-III are capable of providing ~ 10 suitable target stars per year that undergo microlensing events involving passages over the caustic created by a binary lens, which last from a few hours to a few days and allow to resolve the stellar atmosphere by frequent broadband photometry. For a caustic exit lasting 12 h and a photometric precision of 1.5 %, a moderate sampling interval of 30 min (corresponding to ~ 25 –30 data points) is sufficient for providing a reliable measurement of the linear limb-darkening coefficient Γ with an uncertainty of ~ 8 %, which reduces to ~ 3 % for a reduced sampling interval of 6 min for the surroundings of the end of the caustic exit. While some additional points over the remaining parts of the lightcurve are highly valuable, a denser sampling in these regions provides little improvement. Unless an accuracy of less than 5 % is desired, limb-darkening coefficients for several filters can be obtained or observing time can be spent on other targets during the same night. The adoption of an inappropriate stellar brightness profile as well as the effect of acceleration between source and caustic yield distinguishable characteristic systematics in the model residuals. Acceleration effects are unlikely to affect the lightcurve significantly for most events, although a free acceleration parameter blurs the limb-darkening measurement if the passage duration cannot be accurately determined.

Key words: gravitational lensing – stars: atmospheres.

1 INTRODUCTION

The light we receive from a star originates from layers at different depths from its surface, where the contribution of inner layers decreases from the center towards the limb yielding the phenomenon of limb darkening of the observed surface brightness across the stellar face, which reflects the temperature of the stellar atmosphere as function of distance from the center. Decreasing temperatures from the center to the surface cause a stronger effect for shorter wavelengths, making stars bluer near their center and redder near their limb.

Using caustics of gravitational lenses to measure the brightness profile of closely-aligned background sources was proposed by Schneider & Weiß (1987) with the view toward active galactic nuclei, and several authors have later discussed its application to source stars undergoing galactic microlensing events that involve fold-caustic passages (e.g. Rhie & Bennett 1999; Gaudi & Gould 1999). Making use of both the large total magnification and a strong differential magnification across the stellar face during the caustic passage, galactic microlensing has successfully been demonstrated to be a powerful technique for revealing the brightness profile of distant stars by providing several measurements of limb-darkening coefficients characterizing linear or square-root laws

(Albrow et al. 1999a, 2000, 2001; Afonso et al. 2000; Fields et al. 2003; Yoo et al. 2003) with uncertainties of a few percent.

As discussed in detail by Dominik (2003), the lightcurve of a source star in the vicinity of a fold caustic is completely characterized by local properties, so that its brightness profile can be obtained already from data taken around the caustic passage without the need to find a model for the full lightcurve, which describes all properties of the lens system and involves a larger number of parameters along with possible parameter ambiguities. Nevertheless, data outside the caustic passage region provide stronger constraints on the differential blending between observing sites and filters as well as a better assessment of acceleration effects between source and caustic, which can be caused by the parallactic motion of the Earth around the Sun or by orbital motion of the binary lens or a possible binary source. This additional information can be used to reduce uncertainties in the measurement of the stellar brightness profile and its characterizing limb-darkening coefficients.

Some aspects of the measurement of limb-darkening coefficients from microlensing events involving fold-caustic passages have previously been studied by Rhie & Bennett (1999). This article provides a deeper and furthergoing discussion on this issue and on some general properties of lightcurves of microlensed sources near fold caustics with respect to revealing their brightness profiles.

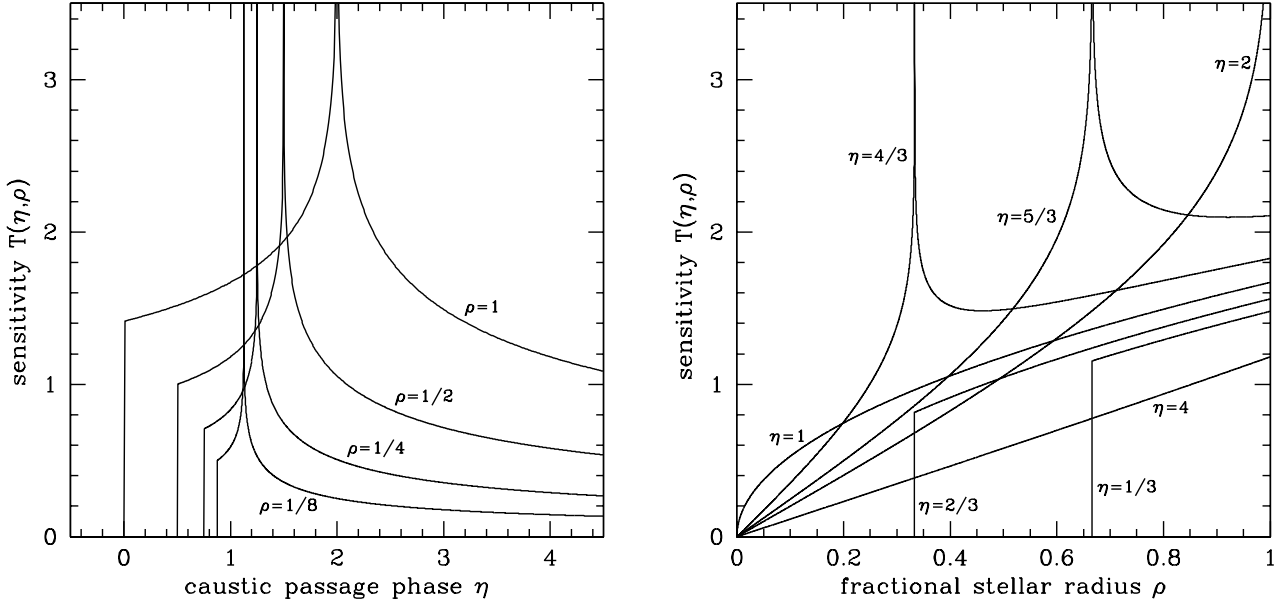


Figure 1. The sensitivity $\mathcal{T}(\eta, \rho)$ of the fold caustic to the shape of the stellar brightness profile ξ as a function of the caustic passage phase $\eta = \pm (t - t_f^*)/t_\star^\perp$ (left) and the fractional stellar radius ρ (right), as given by Eq. (11).

Sect. 2 addresses the relation between the lightcurve and the stellar brightness profile and discusses the sensitivity of microlensing as function of phase during the caustic passage and fractional radius of the source star. With linear limb darkening as example, Sect. 3 deals with parametrized profiles. A simulation of typical sampled data for different sampling rates is described in Sect. 4, which are used in Sect. 5 to investigate the amount of information about the linear limb-darkening coefficient contained in different regions of the lightcurve. In Sect. 6, consequences arising from the adoption of an inadequate limb-darkening profile are discussed, whereas Sect. 7 addresses the influence of an effective acceleration between source and caustic. The paper finishes with a summary of the results and recommendations on the observing strategy in Sect. 8.

2 INTENSITY PROFILE AND LIGHTCURVE

Let us consider a gravitational lens of total mass M at distance D_L from the observer acting on a source at distance D_S . A characteristic scale is then given by the angular Einstein radius

$$\theta_E = \sqrt{\frac{4GM}{c^2} \frac{D_S - D_L}{D_L D_S}}, \quad (1)$$

while its corresponding physical radius at the lens distance is the Einstein radius $r_E = D_L \theta_E$.

With the combined magnification due to the two critical images of a point-like source at a distance $u_\perp \theta_E$ from a fold caustic given by

$$A_{\text{crit}}^p(u_\perp) = \left(\frac{R_f}{u_\perp}\right)^{1/2} \Theta(u_\perp), \quad (2)$$

where R_f describes the caustic strength, $u_\perp > 0$ ($u_\perp < 0$) for a source inside (outside) the caustic, and $\Theta(x)$ is the step function, the corresponding magnification for a circle of angular radius $r\theta_E$ with its center at $u_\perp \theta_E$ reads

$$A_{\text{crit}}^{\text{circle}}(u_\perp, r) = \left(\frac{R_f}{r}\right)^{1/2} j\left(\frac{u_\perp}{r}\right), \quad (3)$$

where

$$j(z) = \begin{cases} 0 & \text{for } z \leq -1 \\ \frac{\sqrt{2}}{\pi} K\left(\sqrt{\frac{1+z}{2}}\right) & \text{for } -1 < z < 1 \\ \frac{2}{\pi \sqrt{1+z}} K\left(\sqrt{\frac{2}{1+z}}\right) & \text{for } z > 1 \end{cases}, \quad (4)$$

and K denotes the complete elliptical integral of first kind (c.f. Gaudi & Gould 1999).

Consider now a star with angular radius $\rho_\star \theta_E$ whose leading limb enters or whose trailing limb exits a fold caustic at time t_f^* and which needs the timespan $2t_\star^\perp$ to cross. The parameter

$$\eta = \pm \frac{t - t_f^*}{t_\star^\perp} = \frac{u_\perp}{\rho_\star} + 1 \quad (5)$$

then describes the phase of the caustic passage, where the upper sign corresponds to a caustic entry and the lower sign corresponds to a caustic exit. The source is completely outside the caustic for $\eta < 0$, completely inside the caustic for $\eta > 2$, and passes the caustic for $0 \leq \eta \leq 2$, where $\eta = 1$ corresponds to the center of the star crossing the caustic. As will be shown in the next section, the reference time t_f^* is preferred over the time $t_f = t_f^* \pm t_\star^\perp$ when the source crosses the caustic, because it can be immediately identified from a distinctive feature in the lightcurve.

With ρ denoting the fractional stellar radius, the stellar brightness profile for a given filter reads

$$I(\rho) = \bar{I} \xi(\rho), \quad (6)$$

where \bar{I} denotes the average surface brightness and $\xi(\rho)$ is a dimensionless function describing the radial profile, so that

$$\int_0^1 \xi(\rho) \rho d\rho = \frac{1}{2}. \quad (7)$$

The magnification of the critical images takes the form

$$A_{\text{crit}}(\eta; \xi) = \left(\frac{R_f}{\rho_*} \right)^{1/2} G_f^*(\eta; \xi), \quad (8)$$

and the characteristic caustic profile function $G_f^*(\eta; \xi)$ can be written as

$$G_f^*(\eta; \xi) = \int_0^1 \mathcal{T}(\eta, \rho) \xi(\rho) d\rho, \quad (9)$$

where $\mathcal{T}(\eta, \rho)$ describes the response produced by the caustic to the brightness profile $\xi(\rho)$. In general, the determination of the brightness profile $\xi(\rho)$ involves an inversion of Eq. (9), which constitutes a Fredholm integral equation of first kind. The solution of this problem is non-trivial and has been discussed in some detail by Heyrovský (2003).

Since

$$A_{\text{crit}}(\eta; \xi) = 2 \int_0^1 A_{\text{crit}}^{\text{circle}} \left(\frac{\eta - 1}{\rho_*}, \rho \rho_* \right) \xi(\rho) \rho d\rho, \quad (10)$$

one finds that

$$\mathcal{T}(\eta, \rho) = 2 \rho^{1/2} j \left(\frac{\eta - 1}{\rho} \right). \quad (11)$$

Eq. (10) reflects the fact that, in order to account for the fraction of light provided by each circle, the surface brightness at the corresponding fractional radius has to be weighted by its circumference, which is proportional to ρ .

The function $\mathcal{T}(\eta, \rho)$ is shown in Fig. 1 as a function of the caustic passage phase η for selected values of the fractional stellar radius ρ , and as a function of the fractional stellar radius ρ for selected values of the caustic passage phase η . As long as the circle corresponding to the fractional radius ρ is outside the caustic, only its non-critical images contribute to its light, so that $\mathcal{T}(\eta, \rho)$ is zero for $\eta < \eta_\rho^{\text{out}} = 1 - \rho$, where the caustic is touched and the sensitivity jumps to the value $(2\rho)^{1/2}$. The sensitivity increases with η for $\eta_\rho^{\text{out}} < \eta < \eta_\rho^{\text{in}}$ until the circle is completely inside the caustic at $\eta_\rho^{\text{in}} = 1 + \rho$, where $\mathcal{T}(\eta, \rho)$ diverges. For $\eta > \eta_\rho^{\text{in}}$, the sensitivity asymptotically approaches zero as $\mathcal{T}(\eta, \rho) \simeq \rho \eta^{-1/2}$.

The sensitivity of the lightcurve to the brightness profile at different fractional radii ρ for a given caustic passage phase η qualitatively depends on whether the source is completely outside the caustic ($\eta < 0$), completely inside the caustic ($\eta = 2$), or in the process of passing it with its center outside ($0 \leq \eta < 1$), inside ($1 < \eta \leq 2$), or at the caustic ($\eta = 1$). For any caustic passage phase η , the sensitivity $\mathcal{T}(\eta, \rho)$ vanishes at the source center ($\rho = 0$), while it vanishes identically for any fractional radius ρ if the source is completely outside the caustic ($\eta < 0$), where none of the corresponding circles have critical images. With parts of the source moving inside while the source center is still outside the caustic ($\eta < 1$), only the outer parts of the source with $\rho > \rho_\eta^{\text{out}} = 1 - \eta$ have non-vanishing sensitivities. $\mathcal{T}(\eta, \rho)$ jumps from zero to $[2(1 - \eta)]^{1/2}$ at the fractional radius ρ_η^{out} and increases towards larger ρ . For the source center being at the caustic ($\eta = 1$), one finds that $\mathcal{T}(1, \rho) \propto \rho^{1/2}$. If the source moves further inside ($1 < \eta \leq 2$), increasing fractional radii subsequently dominate the sensitivity function through their infinite peak at $\rho_\eta^{\text{in}} = \eta - 1$, to which $\mathcal{T}(\eta, \rho)$ rises monotonically for $\rho < \rho_\eta^{\text{in}}$. For $\rho > \rho_\eta^{\text{in}}$, $\mathcal{T}(\eta, \rho)$ shows a monotonic decrease from the infinite peak larger η , while a local minimum exists for smaller η , so that a decrease is followed by an increase towards $\rho = 1$. Finally, for sources completely inside the caustic ($\eta > 2$), $\mathcal{T}(\eta, \rho)$ rises monotonically

with the fractional radius ρ from zero at the source center ($\rho = 0$) to a maximum at the limb ($\rho = 1$) and becomes asymptotically proportional to ρ for large η , for which $\mathcal{T}(\eta, \rho) \simeq \rho \eta^{-1/2}$.

The properties of the brightness profile sensitivity function $\mathcal{T}(\eta, \rho)$ show that photometric observations during the passage of a source star over a fold caustic provide a one-dimensional scan of its brightness profile $\xi(\rho)$, during which each fractional radius ρ is most efficiently probed in different ways on the two occasions where its associated circle touches the caustic, namely at $\eta_\rho^{\text{out}} = 1 - \rho$, where the profile sensitivity function jumps from zero to the finite value $(2\rho)^{1/2}$, and at $\eta_\rho^{\text{in}} = 1 + \rho$, where it becomes infinite. Therefore, outer parts of the source are most efficiently probed near the beginning or the end of the caustic passage, whereas inner parts are most efficiently probed while the center of the source passes the caustic. Influenced by the fact that circles corresponding to larger fractional radii have a larger circumference and therefore contribute more light for the same surface brightness, the integrated sensitivity of the caustic to the brightness profile over the full course of the caustic passage increases with fractional radius, so that data of constant quality would yield more information about the outer than about the inner parts of the source.¹

Rather than $G_f^*(\eta; \xi)$ itself, one observes the lightcurve (e.g. Dominik 2003)

$$m_{\text{fold}}(t) = m_f^* - 2.5 \lg \left\{ 1 + \frac{1}{g_f^*} \left[\left(\frac{\hat{t}}{t_*^\perp} \right)^{1/2} G_f^* \left(\pm \frac{t - t_f^*}{t_*^\perp}; \xi \right) + \hat{G}_{\text{other}}^* (\pm \hat{\omega}_f^* (t - t_f^*), g_f^*) \right] \right\} \quad (12)$$

in the vicinity of the caustic passage, with t_f^* and t_*^\perp as defined above, \hat{t} being an arbitrarily chosen unit time, and m_f^* the observed magnitude at time t_f^* . With $m_S \leq m_f^*$ denoting the intrinsic source magnitude, the parameter g_f^* reads

$$g_f^* = \left(\frac{\rho_*}{R_f} \right)^{1/2} \left(\frac{\hat{t}}{t_*^\perp} \right)^{1/2} 10^{0.4(m_S - m_f^*)}. \quad (13)$$

Finally, \hat{G}_{other}^* describes the temporal variation of the magnification due to images of the source star that do not become critical if it hits the caustic, which is measured by $\hat{\omega}_f^*$ and can be approximated as

$$\begin{aligned} \hat{G}_{\text{other}}^*(\Lambda, \hat{g}) &= \hat{g} (\exp \{ \Lambda / \hat{g} \} - 1) \\ &\simeq \Lambda \quad (|\Lambda / \hat{g}| \ll 1). \end{aligned} \quad (14)$$

The establishment of $G_f^*(\eta; \xi)$, from which the stellar brightness profile $\xi(\rho)$ is to be inferred, therefore requires a determination of the 5 parameters t_f^* , t_*^\perp , m_f^* , g_f^* , and $\hat{\omega}_f^*$ from a fit to the collected data, where in particular, t_f^* and t_*^\perp determine the relation between the caustic passage phase η and the elapsed time t .

3 PARAMETRIZED PROFILES

As an example of a parametrized stellar brightness profile, let us consider the case of linear limb darkening characterized by the coefficient $0 \leq \Gamma \leq 1$, where

¹ For constant exposure time during the caustic passage, larger magnifications however account for a higher photometric precision.

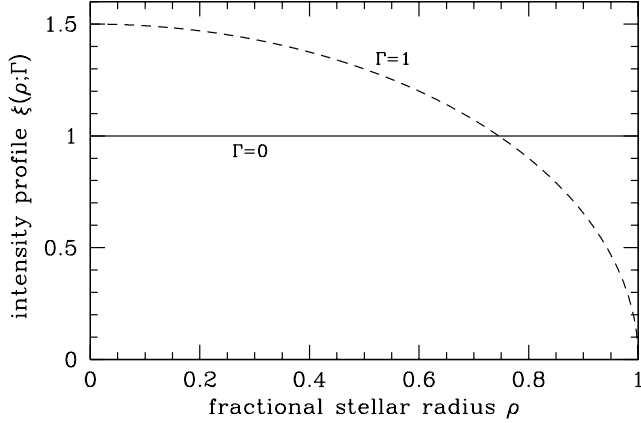


Figure 2. Stellar brightness profiles $\xi(\rho; \Gamma) = (1-\Gamma)\xi_{\{0\}}(\rho) + \Gamma\xi_{\{1\}}(\rho)$ for linear limb darkening as a function of the fractional stellar radius ρ , where the two extreme cases of uniform brightness and maximal limb darkening, corresponding to $\Gamma = 0$ or $\Gamma = 1$, respectively, are shown.

$$\xi(\rho; \Gamma) = (1 - \Gamma)\xi_{\{0\}}(\rho) + \Gamma\xi_{\{1\}}(\rho), \quad (15)$$

with the basis functions

$$\xi_{\{0\}}(\rho) = 1, \quad (16)$$

$$\xi_{\{1\}}(\rho) = \frac{3}{2}\sqrt{1 - \rho^2}. \quad (17)$$

While $\xi_{\{0\}}(\rho)$ corresponds to a uniformly bright source, $\xi_{\{1\}}(\rho)$ is linear in $\cos \vartheta = \sqrt{1 - \rho^2}$, where ϑ denotes the emergent angle. These basis brightness profile functions are displayed in Fig. 2. Any profile $\xi(\rho; \Gamma)$ of the form given by Eq. (15) is a linear superposition of these curves and falls between them.

For such brightness profiles, the caustic profile function reads

$$G_f^*(\eta; \Gamma) = (1 - \Gamma)G_{f,\{0\}}^*(\eta) + \Gamma G_{f,\{1\}}^*(\eta), \quad (18)$$

where $G_{f,\{0\}}^*(\eta)$ and $G_{f,\{1\}}^*(\eta)$ denote the caustic profile functions for the basis stellar brightness profile functions, which can be expressed by means of analytic or semi-analytic functions as (Schneider & Weiß 1987; Schneider & Wagoner 1987; Dominik 2003)

$$G_{f,\{0\}}^*(\eta) = \begin{cases} 0 & \text{for } \eta \leq 0 \\ \frac{4\sqrt{2}}{3\pi} \left[(2 - \eta) K \left(\sqrt{\eta/2} \right) - \right. \\ \quad \left. - 2(1 - \eta) E \left(\sqrt{\eta/2} \right) \right] & \text{for } 0 < \eta < 2 \\ \frac{8}{3\pi} \sqrt{\eta} \left[(2 - \eta) K \left(\sqrt{2/\eta} \right) - \right. \\ \quad \left. - (1 - \eta) E \left(\sqrt{2/\eta} \right) \right] & \text{for } \eta \geq 2 \end{cases}, \quad (19)$$

where K and E denote the complete elliptical integrals of the first or second kind, and

$$G_{f,\{1\}}^*(\eta) = \begin{cases} 0 & \text{for } \eta \leq 0 \\ \frac{2}{5\sqrt{2}\pi} (5 - 2\eta) \eta^{3/2} & \text{for } 0 < \eta \leq 2 \\ \frac{2}{5\sqrt{2}\pi} \left[(5 - 2\eta) \eta^{3/2} + (1 + 2\eta)(\eta - 2)^{3/2} \right] & \text{for } \eta > 2 \end{cases}, \quad (20)$$

respectively, and are shown in Fig. 3 together with their derivatives $G_f^{*'} = dG_f^*/d\eta$ and $G_f^{*''} = d^2G_f^*/d\eta^2$. For any choice of Γ , $G_f^*(\eta; \Gamma)$ vanishes for $\eta \leq 0$, and rises to a peak, which is shifted towards smaller η for stronger limb darkening. Asymptotically, the decrease after the peak behaves as $G_f^*(\eta; \Gamma) \simeq (\eta - 1)^{-1/2}$ regard-

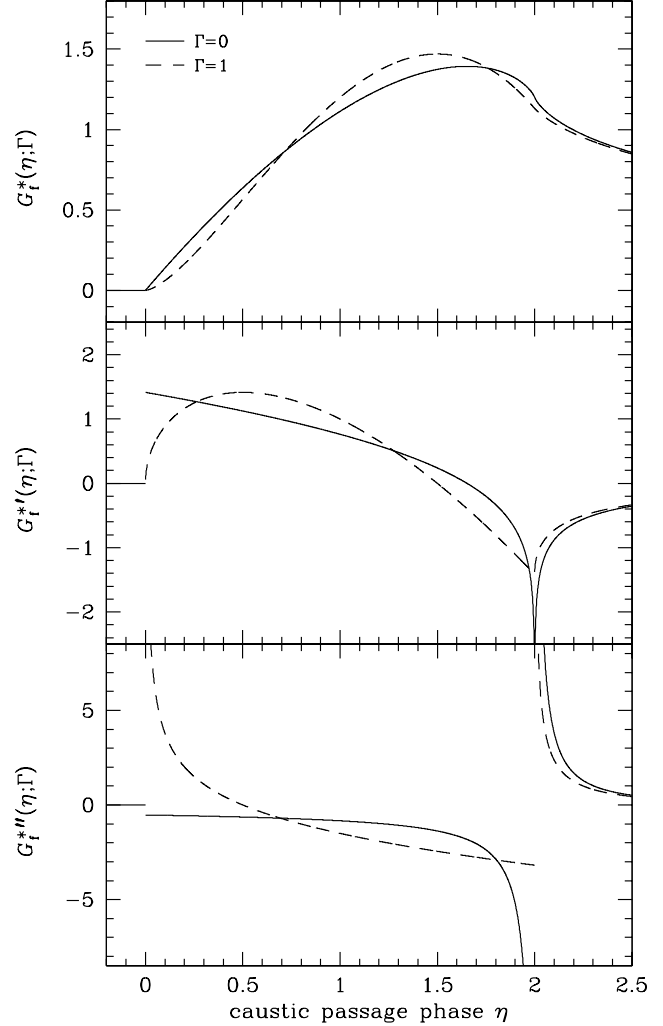


Figure 3. The caustic profile function $G_f^*(\eta; \Gamma) = (1 - \Gamma)G_{f,\{0\}}^*(\eta) + \Gamma G_{f,\{1\}}^*(\eta)$ and its derivatives $G_f^{*'}(\eta; \Gamma)$ and $G_f^{*''}(\eta; \Gamma)$ as a function of the caustic passage phase η . Solid lines correspond to uniform brightness ($\Gamma = 0$) and dashed lines to maximal limb darkening ($\Gamma = 1$), while general profiles with $0 < \Gamma < 1$ fall between these two extreme case.

less of the adopted stellar brightness profile, which corresponds to the behaviour of a point-like source. While the slope of $G_{f,\{1\}}^*(\eta)$ vanishes for $\eta = 0$ and remains finite for $\eta = 2$, it shows a jump discontinuity at $\eta = 0$ and a negative infinite value at $\eta = 2$ for all caustic profiles $G_f^*(\eta; \Gamma)$ with $\Gamma \neq 1$. The trend of initially smaller values of the profile function $G_f^*(\eta; \Gamma)$ and its slope for stronger limb darkening is reversed on the rise to the peak. The slope shows strong variations for small $\eta > 0$ and near $\eta = 2$, and little variation in the remaining regions. For $\eta = 0$, the change of slope with η becomes infinite unless $\Gamma = 0$, for which a finite negative value is taken. Approaching $\eta = 2$ from larger values, the slope of $G_f^*(\eta; \Gamma)$ diverges to positive infinity, whereas it diverges to negative infinity for the approach from smaller values, except for $\Gamma = 1$, where a finite negative value is approached.

A change in the linear limb-darkening coefficient $d\Gamma$ causes the brightness profile $\xi(\rho; \Gamma)$ to vary at each fractional radius ρ by $[\partial\xi(\rho; \Gamma)/\partial\Gamma]d\Gamma$. Due to the linearity of $\xi(\eta; \Gamma)$, $\partial\xi(\rho; \Gamma)/\partial\Gamma$ equals the difference between the basis profiles, i.e.

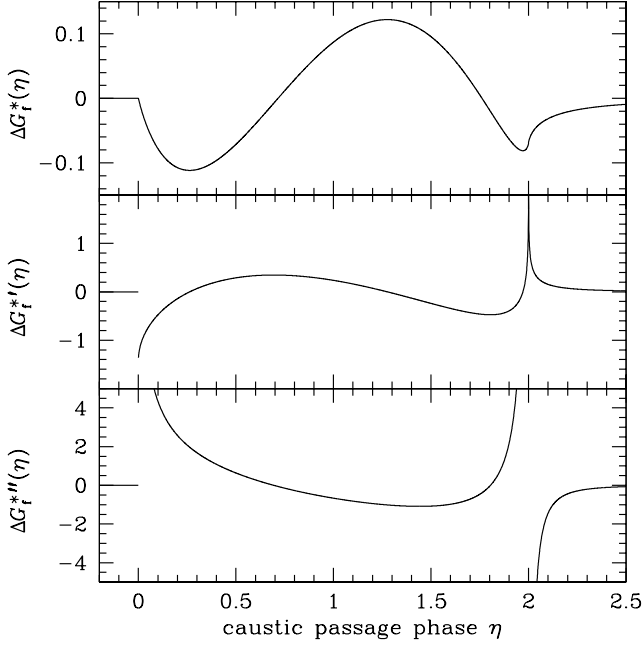


Figure 4. Difference between profile functions $\Delta G_f^*(\eta) = G_{f,\{1\}}^*(\eta) - G_{f,\{0\}}^*(\eta)$ and its derivatives $\Delta G_f^{*'}(\eta)$ and $\Delta G_f^{*''}(\eta)$ measuring the sensitivity of the lightcurve to the limb-darkening coefficient Γ as a function of the caustic passage phase η .

$$\frac{\partial \xi(\rho; \Gamma)}{\partial \Gamma} = \xi_{\{1\}}(\rho) - \xi_{\{0\}}(\rho) \equiv \Delta \xi(\rho), \quad (21)$$

while all higher derivatives of $\xi(\rho; \Gamma)$ vanish identically.² As Fig. 2 shows, $\Delta \xi(\rho)$ decreases monotonically from $\Delta \xi(0) = 1/2$ to $\Delta \xi(1) = -1$. With $d\Delta \xi(\rho)/d\rho = -(3/2)\rho(1-\rho^2)^{-3/2}$, its slope becomes flat at the source center and decreases monotonically towards the limb where it becomes infinite. The normalization forces $\Delta \xi(\rho)$ to change its sign, which occurs for $\rho_0 = \sqrt{5}/3 \approx 0.745$.

Changes in $\xi(\rho; \Gamma)$ caused by variations of Γ alter the caustic profile function $G_f^*(\eta; \Gamma)$ according to Eq. (9) with the sensitivity of the caustic profile at a given passage phase η to these variations characterized by $\mathcal{T}(\eta, \rho)$ as discussed in the previous section. $G_f^*(\eta; \Gamma)$ inherits the linearity in Γ from the brightness profile $\xi(\rho; \Gamma)$, so that

$$\frac{\partial G_f^*(\eta; \Gamma)}{\partial \Gamma} = G_{f,\{1\}}^*(\eta) - G_{f,\{0\}}^*(\eta) \equiv \Delta G_f^*(\eta), \quad (22)$$

measures the sensitivity of the lightcurve to variations of the limb-darkening coefficient Γ and for its derivatives, one finds in analogy $\partial G_f^{*'}(\eta; \Gamma)/\partial \Gamma = \Delta G_f^{*'}(\eta)$ and $\partial G_f^{*''}(\eta; \Gamma)/\partial \Gamma = \Delta G_f^{*''}(\eta)$. These functions are displayed in Fig. 4.

Since the stellar magnitude $m_{\text{fold}}(t)$ is a function of elapsed time t rather than of caustic passage phase η , a reliable measurement of the limb-darkening coefficient Γ requires not only a sufficient sensitivity of the caustic profile function $G_f^*(\eta; \Gamma)$ to the variation of Γ , but in addition also the determination of the parameters t_f^* , t_\star^\perp , m_\star^* , g_\star^* , and $\hat{\omega}_f^*$, which establish the relation between $G_f^*(\eta; \Gamma)$ and $m_{\text{fold}}(t)$, as pointed out in the previous section.

The determination of these parameters from the photometric data over a given region of the lightcurve can be viewed in relation to the local assessment of the caustic profile function $G_f^*(\eta; \Gamma)$ and its derivatives $G_f^{*'}(\eta; \Gamma)$ and $G_f^{*''}(\eta; \Gamma)$ with respect to the caustic passage phase η as well as their derivatives with respect to Γ , namely $\Delta G_f^*(\eta)$, $\Delta G_f^{*'}(\eta)$, and $\Delta G_f^{*''}(\eta)$, where the amount of information provided increases with the absolute value of each of these quantities.

With $\mathcal{T}(\eta, \rho) \geq 0$, the sign change in $\Delta \xi$ at $\rho_0 = \sqrt{5}/3$ causes $\Delta G_f^*(\eta)$ to change its sign at $\eta_0^{\text{out}} = 0.716$ and $\eta_0^{\text{in}} = 1.762$, where $\Delta G_f^*(\eta) < 0$ for $0 < \eta < \eta_0^{\text{out}}$ or $\eta > \eta_0^{\text{in}}$, whereas $\Delta G_f^*(\eta) > 0$ for $\eta_0^{\text{out}} < \eta < \eta_0^{\text{in}}$. A change in Γ causes the largest relative changes in the observed flux at the extrema of ΔG_f^* , which occur at $\eta_{\text{min}}^{\text{out}} = 0.263$, $\eta_{\text{max}} = 1.276$, and $\eta_{\text{min}}^{\text{in}} = 1.971$, i.e. close to the point at which the caustic is touched by the limb of the source located inside.

By means of the sensitivity function $\mathcal{T}(\eta, \rho)$, variations of η during the caustic passage alter the weight given to the different fractional radii ρ and $|\Delta G_f^{*'}(\eta)|$ increases with the absolute variation in $\Delta \xi(\rho)$ for the specific radii that dominate $\mathcal{T}(\eta, \rho)$ for a given caustic passage phase η . With $d\Delta \xi(\rho)/d\rho < 0$ decreasing monotonically from the source center to the limb, and moreover, the caustic producing a weaker response characterized by $\mathcal{T}(\eta, \rho)$ to variations of the brightness profile near the source center, the variations in $\Delta G_f^*(\eta)$ are small for $\eta \sim 1$ and large as $\eta \rightarrow 0$ or $\eta \rightarrow 2$. In fact, Fig. 4 shows that $|\Delta G_f^{*'}(\eta)|$ assumes large values for small positive η and in the close vicinity of $\eta \sim 2$, and becomes infinite at $\eta = 0$ and $\eta = 2$, whereas much smaller values are assumed for the remaining part of the caustic passage, and the variation of $\Delta G_f^{*''}(\eta)$, given by $\Delta G_f^{*''}(\eta)$, behaves in a similar way. Roughly speaking, when comparing different phases of the caustic passage, the largest response to a variation of the limb-darkening coefficient is caused around the time when the stellar limb touches the caustic with the source center being inside ($\eta \sim 2$) with all $\Delta G_f^*(\eta)$, $\Delta G_f^{*'}(\eta)$, and $\Delta G_f^{*''}(\eta)$ assuming reasonably large absolute values or even tending to infinity as $\eta \rightarrow 2$. Next comes the region over which the stellar limb touches the caustic while the source center is outside, where in contrast $|\Delta G_f^{*'}(\eta)|$ decreases to zero as positive $\eta \rightarrow 0$ and vanishes identically for $\eta \leq 0$. In contrast, much smaller effects result while the inner parts of the source pass the caustic, for which both $\Delta G_f^{*'}(\eta)$ and $\Delta G_f^{*''}(\eta)$ are close to zero or $|\Delta G_f^*(\eta)|$ is small if one of the former quantities tends to assume a reasonable non-zero value.

In order to assess the potential of different regions of an observed lightcurve for the measurement of the (linear) limb-darkening coefficient Γ , one needs to consider not only the flux variation with Γ at the corresponding caustic phase, but also the observed flux and its uncertainty. Let F_f^* denote the flux at time t_f^* , so that $m_{\text{fold}}(t) = m_\star^* = -2.5 \lg[F_{\text{fold}}(t)/F_f^*]$. The ratio $Z(\eta)$ between signal-to-noise for flux deviations caused by a variation of the limb-darkening coefficient Γ and signal-to-noise for the flux F_f^* is given by

$$Z(\eta) = \frac{\partial F_{\text{fold}}(t_f^* \pm \eta t_\star^\perp; \Gamma)}{\partial \Gamma} \frac{\sigma_f^*}{F_f^* \sigma}. \quad (23)$$

With the assumption that the flux uncertainties σ follow Poisson statistics, so that $\sigma = \sigma_f^* (F/F_f^*)^{1/2}$, where σ_f^* is the uncertainty of F_f^* , and neglecting the temporal flux variation in non-critical images (i.e. adopting $\hat{\omega}_f^* = 0$), one obtains

$$Z(\eta) = \alpha_\Gamma \frac{\Delta G_f^*(\eta)}{\sqrt{\alpha_\Gamma G_f^*(\eta; \Gamma) + 1}}, \quad (24)$$

² Such a property does not hold for the popular parametrization of linear limb darkening where $\xi(\rho; c) = (1 - c/3)^{-1} (1 - c + c \sqrt{1 - \rho^2})$.

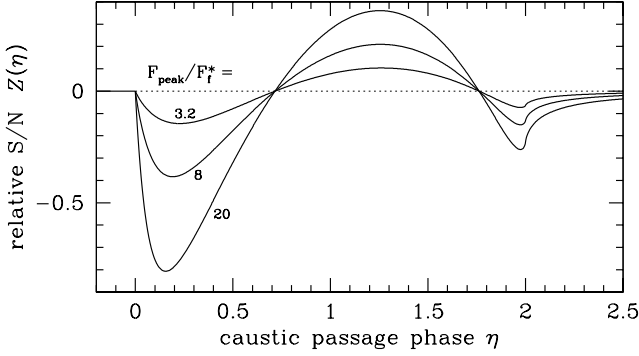


Figure 5. Ratio $Z(\eta)$ between signal-to-noise for the flux variation $[\partial F(t_f^* + \eta t_*^\perp; \Gamma)/\partial \Gamma]/\sigma$ caused by altering the limb-darkening coefficient Γ and signal-to-noise F_f^*/σ_f for the flux measurement outside the caustic for selected caustic-peak-to-outside magnification ratios F_{peak}/F_f^* .

where

$$\alpha_\Gamma = \frac{(F_{\text{peak}}/F_f^*) - 1}{G_{\text{peak},\Gamma}} \quad (25)$$

and $G_{\text{peak},\Gamma}$ is the maximum of $G_f^*(\eta; \Gamma)$ which corresponds to the observed flux F_{peak} .

Using $\Gamma = 1$ as reference, $Z(\eta)$ is shown in Fig. 5 for selected values of the peak-to-outside flux ratio F_{peak}/F_f^* . Compared to the effects on the flux difference as displayed in Fig. 4, caustic passage phases near the beginning of an entry or the end of an exit are favoured, yielding a maximal signal for phases close to – but not at – this point. However, $|\Delta G_f^*(\eta)|$ is small in this region, whereas it peaks for $\eta = 2$, i.e. when the caustic entry is completed or the caustic exit starts.

For $Z(\eta) = 20 (\sigma_f^*/F_f^*)$, a single data point implies an absolute uncertainty of 0.05 for the limb-darkening coefficient Γ . If one considers $F_{\text{peak}}/F_f^* \sim 8$ as for recently observed events, Fig. 5 yields $|Z(\eta)| \sim 0.25$, so that for a photometric precision of a few percent at the caustic outside, tens of data points yield a reliable measurement of Γ .

The identification and assessment of some distinctive characteristic local features in the light curve that do not depend on the stellar brightness profile allow the precise determination of individual lightcurve parameters, leading to a reduction in parameter degeneracies and uncertainties. For any stellar brightness profile that does not vanish at the stellar limb, the slope of the lightcurve exhibits a jump discontinuity at $\eta = 0$ and its identification in the lightcurve directly yields m_f^* and t_f^* . Another distinctive feature for such brightness profiles is the infinite slope and sign change of the curvature at $\eta = 2$, where temporal identification of both $\eta = 0$ and $\eta = 2$ yield t_*^\perp . With $G_f^*(\eta; \Gamma) \equiv 0$ for $\eta < 0$, data taken while the source is completely outside the caustic provide $\hat{\omega}_f$, and with m_f^* and g_f^* can then be measured from the asymptotic form $G_f^*(\eta; \Gamma) \simeq (\eta - 1)^{-1/2}$ for sources inside the caustic. The possibility of measuring each of the parameters t_f^* , m_f^* , and $\hat{\omega}_f$ directly from data obtained around the passage of the stellar limb over the caustic while the source is outside ($\eta \sim 0$) makes this phase of the caustic passage more valuable than that of the limb passage while the source is inside ($\eta \sim 2$), which alone does not provide any direct measurements of individual light curve parameters. Only the combination of both of these phases yields direct measurements of t_*^\perp and g_f^* . In contrast, data taken while the inner parts of the source pass the caustic ($\eta \sim 1$) do not provide any direct measurements of

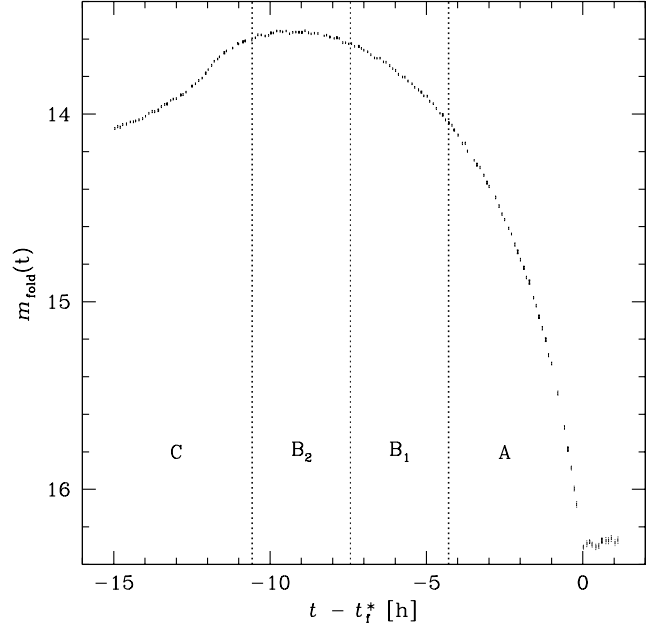


Figure 6. Simulated dataset for the lightcurve parameters $t_f^* = 0$, $t_*^\perp = 6$ h, $m_f^* = 16.3$, $g_f^* = 0.05$ ($\hat{t} = 1$ h), $\hat{\omega}_f^* = -0.001$ h $^{-1}$, and $\Gamma = 0.5$. The standard sampling interval is $\Delta t = 6$ min, while data corresponding to a sparser sampling with $\Delta t = 30$ min only are displayed in bold. The measurement uncertainty has been assumed to be 0.015 mag for m_f^* and scaled to other magnitudes assuming the flux to follow Poisson statistics. More details can be found in the text. The division of the dataset into an outside region A, a central region B, with subregions B₁ and B₂, and an inside region C, is indicated by vertical dashed lines.

lightcurve parameters neither alone nor in combination with data in other regions.

4 SIMULATED PHOTOMETRIC DATA

4.1 Creation of dataset

In order to study the uncertainties of the measurement of the linear limb-darkening coefficient in dependence of the sampling of the lightcurve for different regions, a simulated dataset for a typical caustic exit in accordance with the capabilities of the PLANET campaign (Dominik et al. 2002) has been created. Contrary to caustic entries, which have to be caught by chance, caustic exits can be predicted and therefore provide regular opportunities to obtain high-quality data during caustic passages. For a G/K subgiant in the Galactic bulge at a distance $D_S \sim 8.5$ kpc with a brightness $I \sim 17$ and a radius $R \sim 3 R_\star$, the angular radius becomes $\theta_* \sim 2 \mu\text{as}$, so that the choice of $t_f^* = 6$ h corresponds to a proper motion perpendicular to the caustic of $\mu^\perp \sim 7 \mu\text{as d}^{-1}$ and to a velocity $v^\perp \sim 70$ km s $^{-1}$ at the lens distance $D_L \sim 6$ kpc. For the unit time $\hat{t} = 1$ h and the adopted limb-darkening coefficient $\Gamma = 0.5$, the choice $g_f^* = 0.05$ yields a relative magnification $A_{\text{peak}}/A_f^* \sim 12.5$ of the caustic peak relative to the caustic exit (at time t_f^*), for which we assume $m_f^* = 16.3$. Finally, $\hat{\omega}_f^* = -0.001$ h $^{-1}$ and $t_f^* = 0$ are adopted.

The sampling is characterized by the sampling interval $\Delta t = 6$ min, an uncertainty $\sigma_{\Delta t} = 45$ s of the point of time at which the measurement is taken, and the sampling phase shift $t_{\text{phase}} = 1.2$ min. The uncertainties in the observed magnitudes have been assumed to be $\sigma_0 = 0.015$ at m_f^* (i.e. the relative uncertainty of the

measured flux is $\sim 1.5\%$) and scaled to other magnitudes, so that the uncertainty for the corresponding flux follows Poisson statistics in being proportional to the square-root of its value. Moreover, the uncertainty of the magnitude at given time has been smeared with a relative standard deviation of $f_\sigma = 0.125$.

For $t_{\min} = -15$ h and $t_{\max} = t_{\min} + n \Delta t = 1.2$ h, a synthetic dataset $(t^{(i)}, m^{(i)}, \sigma^{(i)})$ containing $n = 162$ simulated measurements of the time of observation, the magnitude, and its uncertainty has thus been created using

$$t^{(i)} = \mathcal{N}(t_{\min} + i \Delta t + t_{\text{phase}}, \sigma_{\Delta t}), \quad (26)$$

$$\sigma^{(i)} = \mathcal{N}\left(\sigma_0 10^{\{0.2[m_f^* - m_{\text{fold}}(t^{(i)})]\}}, f_\sigma \sigma_0 10^{\{0.2[m_f^* - m_{\text{fold}}(t^{(i)})]\}}\right), \quad (27)$$

$$m^{(i)} = \mathcal{N}(m_{\text{fold}}(t^{(i)}), \sigma^{(i)}), \quad (28)$$

where $\mathcal{N}(\mu, \sigma)$ denotes a value drawn randomly from a normal distribution with mean μ and standard deviation σ .

In order to simulate possible losses in the data acquisition due to observing conditions or technical problems, data points have been removed from the dataset at random with a probability of $q_i = 5\%$. By random selection of data points with a probability of $q_s = 20\%$, a restricted dataset has been obtained, which simulates a sparser sampling with an expected average sampling interval of 30 min. The data used for the subsequent analysis are shown in Fig. 6, with 27 points, which belong to the sparse sampling only shown in bold, while the dense sampling includes all 153 points shown in bold and in light.

Missing or sparse coverage over part of a caustic passage are likely to occur if its duration exceeds the time of coverage possible with a single telescope. Although the coverage by more than one telescope would require different parameters $m_f^{*(s)}$ and $g_f^{*(s)}$ (c.f. Dominik 2003), a careful assessment of parallax between the sites (An et al. 2002), and different achievable photometric precisions, this will be neglected in the following for reasons of simplicity, where site-independent fit parameters m_f^* and g_f^* will be used, which is equivalent to treating the data as resulting from observations with a single telescope.

4.2 Tests on statistical properties

In order to provide a reference and to check the created data set, let us have a look some of its statistics with respect to the underlying set of true parameters \mathbf{p}_{true} .

Let us follow Rhie & Bennett (1999) in using the caustic passage phases at which $\Delta G_f^*(\eta)$ vanishes, namely $\eta_0^{\text{out}} = 0.716$ and $\eta_0^{\text{in}} = 1.762$ as boundaries to divide the data into an outside region A ($\eta < \eta_0^{\text{out}}$), a central region B ($\eta_0^{\text{out}} \leq \eta < \eta_0^{\text{in}}$), and an inside region C ($\eta \geq \eta_0^{\text{in}}$). Furthermore, let us subdivide the central region B at $\eta_0^c = (\eta_0^{\text{out}} + \eta_0^{\text{in}})/2$ into two regions B₁ ($\eta_0^{\text{out}} \leq \eta < \eta_0^c$) and B₂ ($\eta_0^c \leq \eta < \eta_0^{\text{in}}$). These regions are indicated in Fig. 6.

Table 1 gives the number of data points N for the full dataset and each of the regions A, B₁, B₂, and C for both samplings as well as $\chi_{\text{true}}^2 = \chi^2(\mathbf{p}_{\text{true}})$, the ratio χ_{true}^2/N , which is expected to be unity, and the probability $P(\chi^2 \geq \chi_{\text{true}}^2)$. While the standard upper-case letters refer to the simulated data for the dense sampling with $\Delta t = 6$ min, the sparse sampling for a certain region is indicated by the corresponding lower-case letter. One sees that the average absolute size of the residuals differs among the different regions, in particular region B₂ shows rather large residuals while the adjoining region C partly compensates this with smaller than

Table 1. Number of data points N and scatter of residuals for different regions of the simulated dataset.

Region	χ_{true}^2	N	χ_{true}^2/N	$P_{\chi_{\text{true}}^2}$
A	51.5	50	1.02	0.42
B ₁	34.5	31	1.11	0.30
B ₂	42.8	30	1.43	0.06
C	36.7	42	0.87	0.67
ABC	165.5	153	1.08	0.23
a	5.69	11	0.52	0.89
b ₁	3.40	3	1.13	0.33
b ₂	4.38	5	0.88	0.50
c	2.70	8	0.34	0.95
abc	16.17	27	0.60	0.95

$\chi_{\text{true}}^2 = \chi^2(\mathbf{p}_{\text{true}})$ is the value of χ^2 for the true parameters \mathbf{p}_{true} and $P_{\chi_{\text{true}}^2} = P(\chi^2 \geq \chi_{\text{true}}^2)$. Upper-case letters refer to the dense and lower-case letters to the sparse sampling.

expected residuals. At first sight, it might be surprising to find a probability of only about 6% for region B₁. However, this means that the probability that at least one of four regions shows a probability of that order or less is $\sim 25\%$, so that about a quarter of all simulated datasets should share this feature, which is reflected in the probability for the full dataset ABC. The fraction of points selected for the sparse sampling is $\sim 18\%$, somewhat smaller than the expected 20%. In particular, only $\sim 10\%$ of the points in region B₂ made it to b₂. Regions *a* and *c* show residuals whose absolute values are on average much smaller than expected, with a probability of being smaller than this between 5 and 10%. Two regions with probabilities of about 10% make the sparse sample less likely than the dense one with $P(\chi^2 \leq \chi_{\text{true}}^2) \sim 5\%$.

Systematic deviations in the data can be quantitatively assessed by means of a run test, which is based on the statistics of the signs of the residuals irrespective of their absolute values, whereas a χ^2 test is based on the absolute values while being blind to the signs. Let a 'run' being defined as the longest contiguous sequence of residuals with the same sign, and let N denote the total number of data points, N_+ the number of points with positive residuals, and N_- the number of points with negative residuals. For $N > 10$, the distribution of the number of runs n_r can be fairly approximated by a normal distribution with the expectation value

$$\mathcal{E}(n_r) = 1 + \frac{2N_+N_-}{N} \quad (29)$$

and the standard deviation

$$\sigma(n_r) = \sqrt{2N_+N_- \frac{2N_+N_- - N}{N^2(N-1)}}. \quad (30)$$

Results of run tests on the residuals of data in all regions for both adopted samplings with respect to the true lightcurve are listed in Table 2, which do not contradict the assumption that the scatter in the residuals is random.

Without knowledge of the true model parameters, the assessment of the goodness-of-fit by means of χ^2 is hampered by the fact that the reported error bars frequently do not properly reflect the true error bars of the measurement (e.g. Udalski et al. 1994; Albrow et al. 1998) forcing the introduction of modelled scaling factors and/or systematic errors (e.g. Ansari 1994; Dominik 1996; Tsapras et al. 2003), so that the hypothesis of underestimated error bars rather stands against rejecting the model on a basis of a larger

Table 2. Run tests on the lightcurve residuals for the true model parameters.

Region	N	N_+	N_-	$\mathcal{E}(n_r)$	$\sigma(n_r)$	n_r^{obs}	δ	P_r
ABC	153	68	85	76.56	6.09	75	0.26	0.40
abc	27	14	13	14.48	2.54	12	0.98	0.16

From the total number of N data points, N_+ show positive and N_- show negative residuals, implying $\mathcal{E}(n_r)$ runs with a standard deviation $\sigma(n_r)$ to be expected. With n_r^{obs} observed runs, the deviation $\delta = [\mathcal{E}(n_r) - n_r^{\text{obs}}]/\sigma(n_r)$ is related to a probability $P_r = P(n_r \leq n_r^{\text{obs}})$.

than expected χ_{\min}^2 . This is not a problem for the assessment of the run test, which does not depend on the size of the error bars.

5 MEASUREMENT OF PARAMETERS

Without going into much detail, Rhie & Bennett (1999) have stated that a reliable measurement of the limb-darkening coefficient requires a reasonable coverage of the lightcurve in each of the regions A, B, and C. Using the dataset presented in the previous subsections, let us study the information content of each of these regions for the two different realizable sampling rates and the adopted photometric precision that can be expected from the PLANET campaign.

Table 3 gives the parameters obtained by the minimization of χ^2 for the simulated data shown in Fig. 6 in selected regions. The quoted parameter uncertainties δp refer to projections of the hypersurface $\Delta\chi^2 = \chi^2(\mathbf{p}_{\min} + \delta p) - \chi^2(\mathbf{p}_{\min}) = 1$ onto the parameter axes, where \mathbf{p}_{\min} denotes the parameters at the χ^2 minimum $\chi_{\min}^2 = \chi^2(\mathbf{p}_{\min})$, which correspond to intervals containing a probability of 68.3 %. Since the model is not linear in the parameters, upper and lower bounds differ, and 95.4 %-intervals ($\Delta\chi^2 = 4$) are not twice the size of 68.3 %-intervals. Table 4 shows the corresponding values of χ_{\min}^2 , the probability $P_{\chi^2} = P(\chi^2 \geq \chi_{\min}^2)$ indicating the goodness-of-fit, and the χ^2 excess $\Delta\chi_{\text{true}}^2 = \chi^2(\mathbf{p}_{\text{true}}) - \chi^2(\mathbf{p}_{\min})$ of the true parameters \mathbf{p}_{true} with respect to the best-fit parameters \mathbf{p}_{\min} . The values of $\Delta\chi_{\text{true}}^2$ have to be seen with regard to χ_{true}^2 as listed in Table 1 for the different regions of the lightcurve and the average misestimation of error bars indicated by χ_{true}^2/N .

Densely sampled data (every 6 min) for all of the regions (ABC) provide a precise measurement of the limb-darkening coefficient Γ with an uncertainty of $\sim 2.5\%$ and for a sparser sampling (every 30 min) over all regions (abc), the uncertainty still remains below $\sim 6\%$. For the dense (sparse) sampling, the uncertainties on the time t_f^* marking the end of the caustic exit and on the passage half-duration t_{\star}^{\perp} are ~ 30 s (~ 90 s), while the flux at t_f^* is determined within $\sim 0.4\%$ ($\sim 1.5\%$) and the relative uncertainties on g_f and $\hat{\omega}_f^*$ turn out to be $\sim 0.5\%$ ($\sim 2\%$) and $\sim 10\%$ ($\sim 40\%$), respectively.

From data in the outside region A alone, Γ is determined with an uncertainty of $\sim 8\%$. While the slope discontinuity at the end of the caustic exit and the data thereafter provide reliable measurements of t_f^* , m_f^* , and $\hat{\omega}_f^*$ with uncertainties not that much in excess of those for the full dataset, the uncertainties in g_f^* and t_{\star}^{\perp} are largely increased by factors of ~ 20 or ~ 60 , respectively. By combining the outside region A with the inside region C, the latter parameters are accurately determined and the uncertainties on all parameters are close to those for the full dataset (ABC), the uncertainty in Γ being $\sim 4\%$, so that the central region B does not add much valuable information if data in both of the regions A and C are available.

Data taken in each of the inside region C or the central region B alone is insufficient to provide a reliable measurement of the limb-darkening coefficient, where the central region B makes the worse case. However, already a combination of the inside region C with the adjoining half of the central region B₂ yields Γ with an uncertainty of $\sim 10\%$, which improves to $\sim 6\%$ if the full region B is included. The gain in the parameter uncertainties of the other parameters by adding region B₂ to AB₁ is rather moderate, and the uncertainty on the prediction of the caustic exit time t_f^* from data in regions AB₁ is ~ 30 min, while the uncertainty on the corresponding magnitude is ~ 2 mag. Compared to the case in which only data in region A are used, the uncertainties on t_f^* , m_f^* , g_f^* and $\hat{\omega}_f^*$ are at least an order of magnitude larger, while the uncertainty on t_{\star}^{\perp} however is about 3 times smaller.

Although data in region AC provide equal or better constraints than data in region AB or AB₁ for all of the parameters t_f^* , t_{\star}^{\perp} , m_f^* , g_f^* and $\hat{\omega}_f^*$, region AB₁ provides a measurement on Γ of similar quality as region AC, and region AB even provides the same small uncertainty of $\sim 2.5\%$ as the full dataset ABC, making data in region C obsolete in this case. Adding region B₁ to A allows a reliable determination of t_{\star}^{\perp} , and significantly reduces the uncertainty in g_f^* , whereas the uncertainty in t_f^* shows little and those in m_f^* and $\hat{\omega}_f^*$ show no significant improvement. The main gain from region B₂ is in reducing the uncertainty in t_{\star}^{\perp} , whereas m_f^* and $\hat{\omega}_f^*$ as well as their uncertainties remain practically unchanged, and the improvements on t_f^* and g_f^* are quite small to negligible.

With dense sampling of region A yielding an uncertainty of $\sim 8\%$ on Γ and regions B or C being unable to provide a reasonable measurement, none of the regions alone could yield a sufficient accuracy with the sparse sampling. From the combinations of two of these regions, ab yields a marginal limb-darkening measurement with an uncertainty of $\sim 20\%$, while the uncertainty is $\sim 15\%$ for bc and $\sim 10\%$ for ac. Nevertheless, one sees that it is possible to obtain a measurement of the linear limb-darkening coefficient Γ already with a small number of data points with high photometric accuracy over the course of the caustic passage.

The comparison of fits with at most one of the regions A, B, or C being densely and the remaining parts of the source sparsely sampled shows that only dense sampling of region A yields a reasonable reduction of the uncertainty of all parameters, where the uncertainty of the limb-darkening coefficient Γ of $\sim 3\%$ is close to that obtained for the densely sampled full dataset. In contrast, the improvements by increasing the sampling of regions B or C are marginal, although the better sampling of region C yields significant reductions in the uncertainties of t_{\star}^{\perp} , g_f^* and $\hat{\omega}_f^*$.

As for the dense sampling of the outside region A, combining sparsely sampled data in this region with data in one of the other regions is highly valuable, where in contrast to the dense sampling, the inside region (C or c) provides more additional information (in particular through direct measurements of t_{\star}^{\perp} and g_f^*) than the central region (B or b) and coverage of both regions contributes to a significant reduction of the uncertainty on the limb-darkening co-

Table 3. Best-fit parameters and their uncertainties for the simulated data in selected regions of the lightcurve.

Region	t_f^* [h]	t_*^\perp [h]	m_f^*	g_f^*	$-\hat{\omega}_f^*$ [h ⁻¹]	Γ
ABC	$-0.0001^{+0.0091}_{-0.0088}$	$6.0006^{+0.0097}_{-0.0095}$	$16.2967^{+0.0040}_{-0.0040}$	$0.05021^{+0.00025}_{-0.00025}$	$0.00099^{+0.00011}_{-0.00011}$	$0.512^{+0.012}_{-0.012}$
aBC	$-0.007^{+0.017}_{-0.016}$	$5.997^{+0.017}_{-0.016}$	$16.287^{+0.011}_{-0.011}$	$0.05072^{+0.00060}_{-0.00060}$	$0.00099^{+0.00012}_{-0.00011}$	$0.512^{+0.021}_{-0.020}$
Abc	$-0.007^{+0.010}_{-0.010}$	$6.010^{+0.013}_{-0.013}$	$16.2998^{+0.0052}_{-0.0051}$	$0.04975^{+0.00048}_{-0.00048}$	$0.00128^{+0.00032}_{-0.00032}$	$0.522^{+0.016}_{-0.016}$
aBc	$0.00^{+0.020}_{-0.02}$	$6.007^{+0.023}_{-0.024}$	$16.290^{+0.013}_{-0.013}$	$0.05038^{+0.00082}_{-0.00082}$	$0.00120^{+0.00041}_{-0.00037}$	$0.516^{+0.024}_{-0.024}$
abC	$-0.004^{+0.020}_{-0.019}$	$5.987^{+0.019}_{-0.017}$	$16.288^{+0.011}_{-0.011}$	$0.05060^{+0.00061}_{-0.00060}$	$0.00103^{+0.00012}_{-0.00012}$	$0.518^{+0.025}_{-0.025}$
abc	$0.000^{+0.024}_{-0.023}$	$6.007^{+0.025}_{-0.025}$	$16.291^{+0.013}_{-0.013}$	$0.05020^{+0.00085}_{-0.00085}$	$0.00129^{+0.00045}_{-0.00040}$	$0.520^{+0.031}_{-0.030}$
AB ₁	$-0.003^{+0.012}_{-0.011}$	$6.036^{+0.044}_{-0.042}$	$16.3002^{+0.0067}_{-0.0068}$	$0.04941^{+0.00086}_{-0.00082}$	$0.00130^{+0.00051}_{-0.00052}$	$0.499^{+0.020}_{-0.019}$
AB	$0.003^{+0.010}_{-0.010}$	$6.004^{+0.015}_{-0.016}$	$16.3002^{+0.0067}_{-0.0068}$	$0.04981^{+0.00072}_{-0.00066}$	$0.00133^{+0.00052}_{-0.00053}$	$0.512^{+0.013}_{-0.013}$
Ab	$0.009^{+0.010}_{-0.012}$	$5.998^{+0.021}_{-0.021}$	$16.3001^{+0.0066}_{-0.0067}$	$0.04984^{+0.00073}_{-0.00067}$	$0.00133^{+0.00052}_{-0.00053}$	$0.529^{+0.018}_{-0.018}$
aB	$0.062^{+0.099}_{-0.060}$	$5.989^{+0.054}_{-0.049}$	$16.41^{+0.13}_{-0.11}$	$0.0422^{+0.0066}_{-0.0052}$	$0.001^{+0.010}_{-0.008}$	$0.430^{+0.080}_{-0.092}$
ab	$0.07^{+0.09}_{-0.17}$	$5.975^{+0.067}_{-0.046}$	$16.43^{+0.12}_{-0.23}$	$0.0418^{+0.028}_{-0.005}$	$0.011^{+0.010}_{-0.018}$	$0.44^{+0.10}_{-0.09}$
AC	$0.002^{+0.011}_{-0.011}$	$6.001^{+0.011}_{-0.010}$	$16.2970^{+0.0040}_{-0.0040}$	$0.05013^{+0.00027}_{-0.00027}$	$0.00102^{+0.00013}_{-0.00012}$	$0.517^{+0.020}_{-0.020}$
Ac	$0.006^{+0.012}_{-0.012}$	$6.011^{+0.013}_{-0.014}$	$16.3000^{+0.0052}_{-0.0051}$	$0.04970^{+0.00049}_{-0.00049}$	$0.00132^{+0.00034}_{-0.00033}$	$0.521^{+0.021}_{-0.020}$
aC	$-0.023^{+0.024}_{-0.021}$	$5.984^{+0.020}_{-0.017}$	$16.287^{+0.012}_{-0.012}$	$0.05082^{+0.00064}_{-0.00063}$	$0.00095^{+0.00014}_{-0.00013}$	$0.482^{+0.039}_{-0.036}$
ac	$-0.014^{+0.028}_{-0.026}$	$5.998^{+0.026}_{-0.026}$	$16.291^{+0.013}_{-0.013}$	$0.05027^{+0.00088}_{-0.00089}$	$0.00128^{+0.00047}_{-0.00041}$	$0.493^{+0.044}_{-0.042}$
B ₂ C	$0.19^{+0.34}_{-0.61}$	$6.10^{+0.17}_{-0.31}$	$16.7^{+2.7}_{-1.2}$	$0.034^{+0.082}_{-0.032}$	$0.00032^{+0.0045}_{-0.0008}$	$0.494^{+0.054}_{-0.048}$
BC	$0.09^{+0.31}_{-0.46}$	$6.05^{+0.16}_{-0.23}$	$16.6^{+2.3}_{-0.9}$	$0.039^{+0.060}_{-0.035}$	$0.0004^{+0.0032}_{-0.0009}$	$0.523^{+0.032}_{-0.028}$
Bc	$-0.31^{+0.70}_{-0.54}$	$5.86^{+0.35}_{-0.27}$	$15.7^{+2.1}_{-0.6}$	$0.095^{+0.081}_{-0.085}$	$0.0038^{+0.0052}_{-0.0042}$	$0.562^{+0.052}_{-0.049}$
bC	$0.25^{+0.22}_{-0.47}$	$6.13^{+0.12}_{-0.24}$	$17.1^{+2.1}_{-1.3}$	$0.024^{+0.059}_{-0.022}$	$-0.0001^{+0.0029}_{-0.0004}$	$0.521^{+0.038}_{-0.036}$
bc	$0.1^{+0.3}_{-1.1}$	$6.08^{+0.20}_{-0.53}$	$16.5^{+2.3}_{-1.5}$	$0.04^{+0.15}_{-0.04}$	$0.0008^{+0.0095}_{-0.0013}$	$0.545^{+0.063}_{-0.052}$
A	$-0.010^{+0.016}_{-0.015}$	$6.66^{+0.67}_{-0.49}$	$16.3004^{+0.0068}_{-0.0069}$	$0.0425^{+0.0053}_{-0.0058}$	$0.00112^{+0.00048}_{-0.00046}$	$0.466^{+0.044}_{-0.043}$
B	$-0.3^{+1.2}_{-1.1}$	$6.0^{+0.8}_{-1.5}$	$15.3^{+2.0}_{-0.5}$	$0.15^{+0.36}_{-0.14}$	$0.000^{+0.050}_{-0.038}$	$(1 - 10^{-6})^{+10^{-6}}_{-0.59}$
C	$-5.5^{+1.9}_{-0.8}$	$3.30^{+0.94}_{-0.39}$	$14.32^{+0.36}_{-0.14}$	$0.71^{+0.27}_{-0.35}$	$0.031^{+0.017}_{-0.018}$	$0.88^{+0.12}_{-0.30}$

The simulated data are shown in Fig. 6 and corresponds to the true parameters $t_f^* = 0$, $t_*^\perp = 6$ h, $m_f^* = 16.3$, $g_f^* = 0.05$ ($\hat{t} = 1$ h), $\hat{\omega}_f^* = -0.001$ h⁻¹, and $\Gamma = 0.5$. The letter A denotes the outside region ($\eta < \eta_0^{\text{out}}$), B denotes the central region ($\eta_0^{\text{out}} \leq \eta < \eta_0^{\text{in}}$), and C denotes the inside region ($\eta \geq \eta_0^{\text{in}}$), with region B subdivided into B₁ ($\eta_0^{\text{out}} \leq \eta < \eta_c$) and B₂ ($\eta_c \leq \eta < \eta_0^{\text{in}}$), where ΔG_f^* vanishes at $\eta_0^{\text{out}} = 0.716$ and $\eta_0^{\text{in}} = 1.762$, and $\eta_c = (\eta_0^{\text{out}} + \eta_0^{\text{in}})/2$. Upper-case letters refer to the dense sampling ($\Delta t = 6$ min), while corresponding lower-case letters refer to the sparse sampling ($\Delta t = 30$ min). The quoted uncertainties refer to intervals enclosing a probability of 68.3 %.

efficient Γ . For both samplings of the outside region, most of the additional information contained in the other regions is already extracted with the sparse sampling. In all cases, the sampling rate in region A strongly affects the accuracy to which all parameters can be determined.

With data only in the inside and the central region being observed, a denser sampling of the inside region strongly reduces the parameter uncertainties while a denser sampling of the central region has very little effect.

6 INAPPROPRIATE BRIGHTNESS PROFILES

If an inappropriate brightness profile is adopted, the residuals of the data with respect to the model lightcurve show characteristic systematic trends. These are shown in Fig. 7 for models of the full simulated dataset displayed in Fig. 6 where the linear limb-darkening coefficient has been fixed at $\Gamma = 0.3$ or $\Gamma = 0.7$, respectively, whereas $\Gamma = 0.5$ marks its true value. The largest residuals occur near the end of the caustic passage and there are long sequences for which all data points either show larger or smaller magnifications than the theoretical curve. In particular, all data points near the time where the central parts of the source passes deviate to one

side, whereas points where outer parts of the source pass deviate to the other side. The sign of the residuals is just inverted for the two cases $\Gamma = 0.3$ and $\Gamma = 0.7$, representing a too weak or a too strong linear limb-darkening term, respectively.

The parameters and their uncertainties for these two models and corresponding models for the sparse sampling are shown in Table 5. One sees that the achievement of the best-possible fit with the wrong brightness profile leads to an inappropriate choice of the caustic passage half-duration t_*^\perp and the point of time t_f^* when the trailing limb of the source exits the caustic, where t_*^\perp is underestimated and t_f^* is shifted towards the caustic inside for a weaker limb darkening ($\Gamma = 0.3$), whereas t_*^\perp is overestimated and t_f^* is shifted towards the caustic outside for a stronger limb darkening ($\Gamma = 0.7$). The remaining parameters m_f^* , g_f^* , and $\hat{\omega}_f^*$ are fairly reproduced.

There is no significant difference in the residuals between either of the two adopted samplings being applied to the different regions of data. The same systematic trends still persist even if only data in the outside region A are modelled, although the size of the residuals is decreased compared to modelling the full dataset.

Table 6 shows the results of both χ^2 - and run tests for the models with fixed limb-darkening coefficient of the data corresponding to the two different samplings. The larger number of data points for

Table 5. Best-fit model parameters for the simulated dataset with fixed inappropriate limb-darkening coefficient.

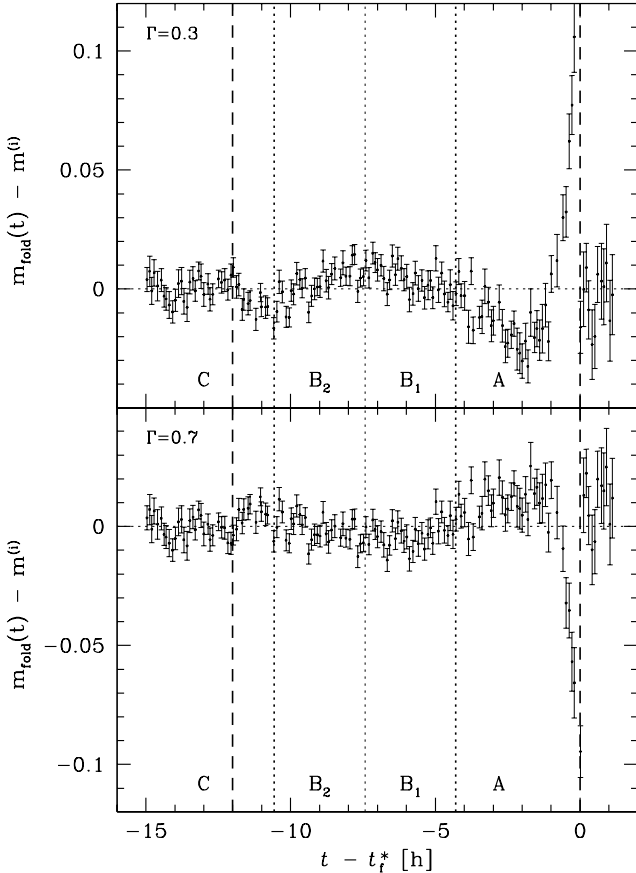
Γ	Region	t_f^* [h]	t_*^\perp [h]	m_f^*	g_f^*	$-\dot{\omega}_f^*$ [h $^{-1}$]
0.3	ABC	$-0.1215^{+0.0037}_{-0.0037}$	$5.8791^{+0.0051}_{-0.0051}$	$16.2950^{+0.0041}_{-0.0041}$	$0.05030^{+0.00026}_{-0.00026}$	$0.00100^{+0.00011}_{-0.00011}$
0.3	abc	$-0.138^{+0.011}_{-0.011}$	$5.870^{+0.019}_{-0.019}$	$16.286^{+0.014}_{-0.013}$	$0.0507^{+0.0010}_{-0.0010}$	$0.00111^{+0.00052}_{-0.00044}$
0.7	ABC	$0.1259^{+0.0046}_{-0.0045}$	$6.1239^{+0.0060}_{-0.0060}$	$16.3028^{+0.0041}_{-0.0041}$	$0.04992^{+0.00025}_{-0.00025}$	$0.00094^{+0.00011}_{-0.00011}$
0.7	abc	$0.128^{+0.012}_{-0.012}$	$6.124^{+0.018}_{-0.017}$	$16.292^{+0.012}_{-0.012}$	$0.05026^{+0.00080}_{-0.00082}$	$0.00115^{+0.00045}_{-0.00039}$

Models with $\Gamma = 0.3$ or $\Gamma = 0.7$ using the full simulated dataset corresponding to dense sampling (ABC) or the reduced dataset corresponding to sparse sampling (abc). The quoted uncertainties correspond to 68.3 % confidence intervals.

Table 6. χ^2 - and run test for models with a fixed inappropriate limb-darkening coefficient.

Γ	Region	χ_{\min}^2	d.o.f.	P_{χ^2}	N	N_+	N_-	$\mathcal{E}(n_r)$	$\sigma(n_r)$	n_r^{obs}	δ	P_r
0.3	ABC	566.7	148	2.8×10^{-120}	153	77	76	77.50	6.16	48	4.79	8.3×10^{-7}
0.3	abc	79.3	22	8.0×10^{-10}	27	10	17	13.59	2.37	7	2.78	2.7×10^{-3}
0.7	ABC	419.6	148	1.8×10^{-62}	153	81	72	77.24	6.14	51	4.27	9.8×10^{-6}
0.7	abc	39.3	22	0.013	27	19	8	12.26	2.11	10	1.07	0.14

Minimization of χ^2 yielded χ_{\min}^2 for the listed models, which corresponds to a probability $P_{\chi^2} = P(\chi^2 \geq \chi_{\min}^2)$. Run tests for the same models and N data points within the specified region revealed N_+ positive and N_- negative residuals forming n_r^{obs} runs, where $\mathcal{E}(n_r)$ runs are expected with a standard deviation $\sigma(n_r)$. The discrepancy $\delta = [\mathcal{E}(n_r) - n_r^{\text{obs}}]/\sigma(n_r)$ corresponds to a probability $P_r = P(n_r \leq n_r^{\text{obs}})$.

**Figure 7.** Residuals of data with respect to model lightcurves for (incorrect) stellar brightness profiles with $\Gamma = 0.3$ and $\Gamma = 0.7$, where the true value of the underlying simulated dataset (as shown in Fig. 6) is $\Gamma = 0.5$.**Table 4.** χ^2 test on models based on data in different regions and corresponding χ^2 excess of true parameters.

Region	χ_{\min}^2	d.o.f.	P_{χ^2}	$\Delta\chi_{\text{true}}^2$
ABC	160.1	147	0.22	5.4
aBC	115.8	108	0.29	3.9
Abc	54.7	60	0.67	7.3
aBc	82.2	74	0.24	4.5
abC	46.2	55	0.80	4.0
abc	12.0	21	0.94	4.2
AB ₁	80.6	75	0.31	5.4
AB	123.2	105	0.11	5.6
Ab	55.1	52	0.36	7.6
aB	78.3	66	0.14	4.7
ab	8.4	13	0.82	5.1
AC	83.4	86	0.56	4.8
Ac	48.8	52	0.60	5.4
aC	39.1	47	0.79	3.3
ac	5.6	13	0.96	2.8
B ₂ C	77.9	66	0.15	1.6
BC	111.9	97	0.14	2.2
Bc	77.4	63	0.11	2.6
bC	41.7	44	0.57	2.8
bc	7.5	10	0.68	3.0
A	44.4	44	0.45	7.0
B	74.3	55	0.04	3.0
C	32.3	36	0.65	4.5

The probability $P_{\chi^2} = P(\chi^2 \geq \chi_{\min}^2)$ provides a measure of the goodness-of-fit, while $\Delta\chi_{\text{true}}^2 = \chi^2(\mathbf{p}_{\text{true}}) - \chi^2(\mathbf{p}_{\min})$ gives the excess in χ^2 of the true parameter set \mathbf{p}_{true} over the best-fit parameter set \mathbf{p}_{\min} .

the dense sampling strongly increases the significance and each of the tests clearly recommends rejection of both of the models with $\Gamma = 0.3$ and $\Gamma = 0.7$. For the sparse sampling, this the case only for the model with $\Gamma = 0.3$, whereas the model with $\Gamma = 0.7$

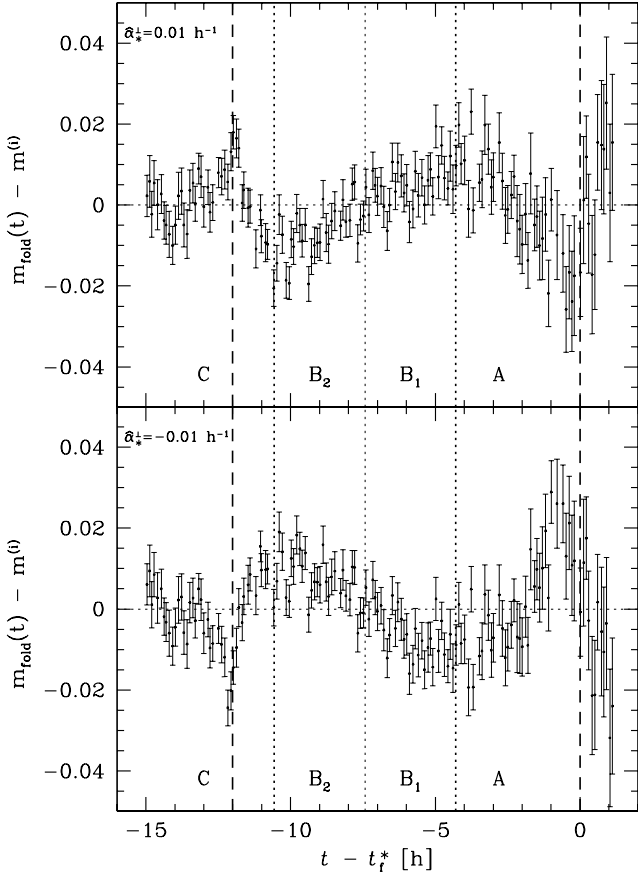


Figure 8. Residuals of data with respect to model lightcurves with fixed (incorrect) acceleration parameters $\hat{\alpha}_*^\perp = 0.01 \text{ h}^{-1}$ and $\hat{\alpha}_*^\perp = -0.01 \text{ h}^{-1}$, where the true value of the underlying simulated dataset (as shown in Fig. 6) is $\hat{\alpha}_*^\perp = 0$.

might be accepted. The χ^2 tests turn out to be more powerful than the run tests for all models. The power of the latter is limited by the requirement that subsequent systematic deviations to the same side need to be established for each of the regions over which they persist separately, while the use of the sum of the squared deviations in χ^2 tests exploits the power of the total number of data points, which can become quite large for $N \gtrsim 100$. However, as pointed out in Sect. 4.2, the uncertainty in the size of the true error bars limits the power of rejecting models by means of a χ^2 test.

While stellar brightness profiles described by a linear limb-darkening law have been studied in detail in this section, it is obvious that other profiles show a similar behaviour if the strength of limb darkening is under- or overestimated.

7 ACCELERATION EFFECTS

7.1 Origin and order estimates

The revolution of the Earth around the Sun and the orbital motion of the binary lens or a possible binary source (Dominik 1998; Smith, Mao & Paczyński 2003) cause an effective acceleration between lens and caustic, which leads to a modified relation between the caustic passage phase η and the elapsed time t , namely

$$\eta = \pm \frac{t - t_f^*}{t_*^\perp} \frac{1}{1 + \hat{\alpha}_*^\perp t_*^\perp} \left[1 \pm \frac{\hat{\alpha}_*^\perp}{2} (t - t_f^*) \right]. \quad (31)$$

This definition preserves the caustic passage taking place for $0 \leq \eta \leq 2$ and lasting $2t_*^\perp$. The proper motion of the source perpendicular to the caustic reads

$$\mu^\perp(t) = \mu_f^* \left[1 + \hat{\alpha}_*^\perp (t - t_f^*) \right], \quad (32)$$

where $\mu_f^* = \mu^\perp(t_f^*)$ and with the constant acceleration $\dot{\mu}^\perp$, the acceleration parameter $\hat{\alpha}_*^\perp$ is defined as $\hat{\alpha}_*^\perp = \dot{\mu}^\perp / \mu_f^*$. For $\hat{\alpha}_*^\perp < 0$, the source will reverse its direction of motion for sufficiently large t where $\mu^\perp(t)$ becomes zero. Requiring that the source does not move in opposite directions at $t_f^* \pm 2t_*^\perp$ and t_f^* implies the restriction $\hat{\alpha}_*^\perp \geq -1/(2t_*^\perp)$ and ensures that $t_f^* \pm 2t_*^\perp$ is the earlier time for which $\eta = 2$ is reached.

For microlensing observations toward the Galactic bulge, let us adopt source and lens distances of $D_S \sim 8.5 \text{ kpc}$ and $D_L \sim 6 \text{ kpc}$, respectively. With the Earth's velocity of $v_\oplus \sim 30 \text{ km s}^{-1}$, a change of the relative proper motion perpendicular to the caustic of $\dot{\mu}_\oplus^\perp = \kappa_\oplus^\perp \frac{D_S - D_L}{D_L D_S} (v_\oplus^2 / (1 \text{ AU})) \sim 1.5 \times 10^{-2} \mu\text{as d}^{-1}$ is induced, where $\kappa_\oplus^\perp \leq 1$ is a geometrical projection factor depending on the angles between the Earth's acceleration vector and the line-of-sight and between its projection perpendicular to the line-of-sight and the relative proper motion between source and caustic. For a relative perpendicular proper motion of $\mu^\perp \sim 10 \mu\text{as d}^{-1}$, corresponding to a velocity of $v^\perp = D_L \mu^\perp \sim 100 \text{ km s}^{-1}$ at the position of the lens, the acceleration parameter becomes $\hat{\alpha}_{*,\oplus}^\perp = \dot{\mu}_\oplus^\perp / \mu^\perp \sim 4 \times 10^{-5} \kappa_\oplus^\perp \text{ h}^{-1}$.

The orbital motion of a binary lens causes a rotation of its caustic with its orbital period and an alteration of shape and strength due to changes in the angular separation between its constituents. For a total mass $M \sim 0.7 M_\odot$ and semi-major axis $a \sim 1.6 \text{ AU}$, the orbital period becomes $P \sim 2.4 \text{ yr}$, the Einstein radius for $D_S \sim 8.5 \text{ kpc}$ and $D_L \sim 6 \text{ kpc}$ is $r_E \sim 3.1 \text{ AU}$, and the angular Einstein radius is $\theta_E \sim 0.54 \text{ mas}$. For moderate eccentricities, the orbital acceleration does not differ much from that for circular orbits. Depending on the orbital inclination and phase, the separation between the constituents of the binary lens falls into the range $0 \leq r_p \leq a$, where $r_p = a$ for all times in face-on orbits. Since $a \sim 0.51 r_E$, the lens is a close binary with respect to its caustic topology for any mass ratio q , showing a diamond-shaped caustic at its center-of-mass (Erdl & Schneider 1993; Dominik 1999). The acceleration induced by the rotation for a point on the caustic located at an angle θ from the center-of-mass reads $\dot{\mu}_{\text{rot}}^\perp = 4\pi^2 \kappa_{\text{rot}}^\perp (r_p/a) P^{-2} \theta$, where the factor r_p/a accounts for the projection of the orbital motion onto the sky, while the geometrical factor $\kappa_{\text{rot}}^\perp \leq 1$ is related to the angle between the projected acceleration vector and the proper motion between source and caustic. For a mass ratio $q \sim 0.8$ and $r_p = a$, the angular extent of the caustic is $\sim 0.26 \theta_E$ (Dominik 1999), and for a source intersecting the caustic at $\theta \sim 0.1 \theta_E$, the angular acceleration perpendicular to the caustic becomes $\dot{\mu}_{\text{rot}}^\perp = 2.7 \times 10^{-3} \kappa_{\text{rot}}^\perp \mu\text{as d}^{-1}$, so that $\mu^\perp \sim 10 \mu\text{as d}^{-1}$ implies an acceleration parameter of $\hat{\alpha}_{*,\text{rot}}^\perp \sim 10^{-5} \kappa_{\text{rot}}^\perp \text{ h}^{-1}$.

While face-on orbits provide the largest effect on the acceleration from the rotation, the alteration of the angular separation of the constituents is largest for edge-on orbits and causes the size of the caustic to change proportional to $d^2 = (r_p/r_E)^2$. With $(d^2/dt^2)d^2 = 2(d\dot{d} + \dot{d}^2)$ and $d(t) = (a/r_E) \cos[(2\pi/P)t + \varphi_0]$ for a circular edge-on orbit, the induced acceleration for a point on the caustic at angle θ reads $\dot{\mu}_{\text{osc}}^\perp = 8\pi^2 \kappa_{\text{osc}}^\perp P^{-2} \theta$, which becomes $\dot{\mu}_{\text{osc}}^\perp = 5.4 \times 10^{-3} \kappa_{\text{osc}}^\perp \mu\text{as d}^{-1}$ for the parameters chosen above, so that the acceleration parameter becomes $\hat{\alpha}_{*,\text{osc}}^\perp \sim 2 \times 10^{-5} \kappa_{\text{osc}}^\perp \text{ h}^{-1}$, where the geometrical factor $\kappa_{\text{osc}}^\perp \leq 1$ accounts

Table 7. Estimates for the correlation coefficient between residuals and elapsed time.

Γ	$\hat{\alpha}_*^\perp$	$\hat{\rho}_1$	$\hat{\rho}_2$	z_1	z_2	$\hat{\rho}^+$	$\hat{\rho}^-$	z^+	z^-
0.3	0	-0.59	0.62	-0.61	-0.68	<i>0.02</i>	-0.61	<i>-0.03</i>	-0.70
0.7	0	0.23	-0.42	0.23	-0.45	<i>-0.10</i>	0.32	<i>-0.11</i>	0.34
0.5	0.01	0.38	0.55	0.40	0.62	0.46	<i>-0.09</i>	0.51	<i>-0.11</i>
0.5	0.003	<i>0.03</i>	0.24	<i>0.03</i>	0.25	0.14	<i>-0.11</i>	0.14	<i>-0.11</i>
0.5	0.001	<i>-0.08</i>	<i>-0.13</i>	<i>-0.08</i>	<i>-0.13</i>	<i>0.02</i>	<i>-0.11</i>	<i>0.02</i>	<i>-0.11</i>
0.5	-0.01	-0.61	-0.49	-0.70	-0.54	-0.55	<i>-0.06</i>	-0.62	<i>-0.08</i>
0.5	-0.003	-0.32	<i>-0.11</i>	-0.33	<i>-0.11</i>	-0.22	<i>-0.10</i>	-0.22	<i>-0.11</i>
0.5	-0.001	-0.20	<i>0.01</i>	-0.20	<i>0.01</i>	<i>-0.10</i>	<i>-0.10</i>	<i>-0.10</i>	<i>-0.11</i>

For models involving the full dataset over regions A, B, and C, the estimated correlation coefficients $\hat{\rho}_1$ and $\hat{\rho}_2$ correspond to data in the subregions B₁ and B₂, while $\hat{\rho}^\pm = (\hat{\rho}_1 \pm \hat{\rho}_2)/2$ give the antisymmetrized or symmetrized correlation for the full region B. Symmetry is indicated by a vanishing $\hat{\rho}^+$, while a vanishing $\hat{\rho}^-$ indicates antisymmetry. With $N_1 = 31$ data points in the region B₁ and $N_2 = 30$ data points in the region B₂, the standard deviation on $z_{1,2} = 0.5 \ln[(1 + \hat{\rho}_{1,2})/(1 - \hat{\rho}_{1,2})]$, is $\sigma_{z_1} \approx \sigma_{z_2} \approx 0.19$ and the standard deviation on $z^\pm = (z_1 \pm z_2)/2$ is $\sigma_{z^\pm} \approx 0.13$. Values that are compatible with zero within one standard deviation are shown in *italics*.

for the orbital phase and inclination as well as for the caustic crossing angle.

The effective acceleration caused by orbital motion strongly increases towards shorter binary periods, however, in order to intersect the increasingly smaller caustics, smaller impact parameters are required, which are less likely to occur. Larger acceleration effects are therefore not impossible but rather improbable. In general, the contributions of parallax and the rotational and oscillatory contributions by orbital motion are roughly of competitive order.

7.2 Signature of acceleration

In order to cause deviations of 1–2 %, the acceleration parameter needs to exceed $|\hat{\alpha}_*^\perp| \gtrsim 0.01 \text{ h}^{-1}$ for the parameters $g_f^* = 0.05$ ($\hat{t} = 1 \text{ h}$) and $t_f^* = 6 \text{ h}$, which have been chosen for the simulated dataset, and is therefore required to be much larger than the expected values, indicating that effective acceleration is unlikely to play an important role. The influence of acceleration increases with

$$\begin{aligned}
 f_{\text{acc}} &\propto \hat{\alpha}_*^\perp (t_*^\perp)^{1/2} (g_f^*)^{-1} \\
 &\propto \hat{\alpha}_*^\perp t_*^\perp \theta_*^{-1/2} 10^{-0.4(m_S - m_f^*)} \\
 &= \hat{\alpha}_*^\perp (t_*^\perp / \mu^\perp)^{1/2} 10^{-0.4(m_S - m_f^*)}, \quad (33)
 \end{aligned}$$

so that stronger effects occur for longer passage half-durations t_*^\perp in combination with smaller angular stellar radii θ_* or smaller proper motions μ^\perp , as well as for larger caustic strength R_f , although a very large increase is not likely to occur, whereas a decrease results from larger $m_S - m_f^*$, i.e. larger magnification at t_f^* .

The residuals for models with $\hat{\alpha}_*^\perp = \pm 0.01 \text{ h}^{-1}$, as shown in Fig. 8, exhibit characteristic systematic trends, which can be distinguished from those occurring with the adoption of an inappropriate stellar brightness profile. For the latter case, the residuals during the central part of the caustic passage (region B) are roughly symmetric with respect to the boundary between the subregions B₁ and B₂ while deviations to one side dominate for adjoining parts of the limb regions A and C, and just the very outer limb in region A shows a strong deviation to the same side as the central part of region B. In contrast, the residuals for models including an inappropriate assumed acceleration are roughly antisymmetric about the temporal midpoint for each of the regions A, B, and C, showing a linear trend and reaching maxima at about the boundaries of these regions and the endpoints of the caustic passage. Therefore, tests of symmetry or antisymmetry in the different regions can be used to

decide whether model discrepancies are due to acceleration effects or the adoption of inappropriate brightness profiles.

For N data points (x_i, y_i) , where $1 \leq i \leq N$, an estimate for the correlation coefficient $-1 \leq \hat{\rho} \leq 1$ is obtained as

$$\hat{\rho} = \frac{N \sum x_i y_i - \sum x_i \sum y_i}{\sqrt{[N \sum x_i^2 - (\sum x_i)^2] [N \sum y_i^2 - (\sum y_i)^2]}}, \quad (34)$$

where Fisher's transform

$$z = \frac{1}{2} \ln \frac{1 + \hat{\rho}}{1 - \hat{\rho}} \quad (35)$$

asymptotically follows a normal distribution around its expectation value with standard deviation $\sigma_z = 1/\sqrt{N-3}$.

For the subregions B₁ and B₂, estimates for the correlation coefficient, $\hat{\rho}_1$ and $\hat{\rho}_2$, and the corresponding values of Fisher's transform, z_1 and z_2 , have been calculated for the previously discussed models involving an incorrect brightness profile or acceleration parameter based on the complete dataset ABC. The antisymmetrized or symmetrized correlation over the whole region B is characterized by $\hat{\rho}^\pm = (\hat{\rho}_1 \pm \hat{\rho}_2)/2$ and $z^\pm = (z_1 \pm z_2)/2$ with $\sigma_{z^\pm} = 0.5 \sqrt{(N_1 + N_2 - 6)/[(N_1 - 3)(N_2 - 3)]}$. For a symmetry (as for an incorrect brightness profile), one expects $\hat{\rho}^+$ to vanish, while $\hat{\rho}^-$ is expected to vanish for an antisymmetry (as for an incorrect acceleration parameter), whereas signatures of a symmetry or antisymmetry are obtained from values that significantly differ from zero. The obtained values are displayed in Table 7, where entries in *italics* are compatible with zero within the standard deviation. The obtained estimates for the correlation coefficient reflect the expected behaviour and allow to distinguish between the two different causes of systematic residuals unless the random scatter of the residuals dominates over the systematic trend, which is the case for $|\hat{\alpha}_*^\perp| = 0.001 \text{ h}^{-1}$, where both $\hat{\rho}^+$ and $\hat{\rho}^-$ are compatible with zero.

The model parameters and their 68.3 % confidence intervals are shown in Table 8. One sees that larger acceleration parameters yield smaller limb-darkening coefficients Γ , shorter caustic passage half-durations t_*^\perp , smaller $\hat{\omega}_f^*$ and larger g_f^* , whereas smaller acceleration parameters alter the estimates for Γ , t_*^\perp , $\hat{\omega}_f^*$, and g_f^* in the opposite direction.

While probabilities corresponding to χ^2 as shown in Table 9 reveal the incompatibility of the model with the data for the selected values of $\hat{\alpha}_*^\perp = \pm 0.01 \text{ h}^{-1}$ and $\hat{\alpha}_*^\perp = \pm 0.003 \text{ h}^{-1}$ due to the size of the absolute deviations, the results of a run test show the presence of systematic trends for $\hat{\alpha}_*^\perp = \pm 0.01 \text{ h}^{-1}$. As can be seen

Table 8. Best-fit model parameters obtained for selected fixed acceleration parameters.

$\hat{\alpha}_*^\perp$ [h^{-1}]	Region	t_f^* [h]	t_*^\perp [h]	m_f^*	g_f^*	$-\hat{\omega}_f^*$ [h^{-1}]	Γ
0.01	ABC	$-0.0044^{+0.0080}_{-0.0086}$	$5.9103^{+0.0090}_{-0.0087}$	$16.2916^{+0.0039}_{-0.0039}$	$0.05073^{+0.00024}_{-0.00024}$	$0.000228^{+0.000084}_{-0.000082}$	$0.423^{+0.011}_{-0.011}$
0.003	ABC	$-0.0005^{+0.0092}_{-0.0089}$	$5.9731^{+0.0098}_{-0.0096}$	$16.2951^{+0.0040}_{-0.0040}$	$0.05037^{+0.00024}_{-0.00025}$	$0.00073^{+0.00010}_{-0.00010}$	$0.485^{+0.012}_{-0.012}$
0.001	ABC	$0.0003^{+0.0088}_{-0.0082}$	$5.9919^{+0.0091}_{-0.0083}$	$16.2962^{+0.0040}_{-0.0040}$	$0.05026^{+0.00024}_{-0.00024}$	$0.00090^{+0.00011}_{-0.00010}$	$0.503^{+0.012}_{-0.012}$
-0.01	ABC	$0.013^{+0.010}_{-0.010}$	$6.123^{+0.011}_{-0.012}$	$16.3076^{+0.0045}_{-0.0044}$	$0.04903^{+0.00031}_{-0.00032}$	$0.00248^{+0.00022}_{-0.00021}$	$0.612^{+0.013}_{-0.014}$
-0.003	ABC	$-0.0009^{+0.0096}_{-0.0080}$	$6.029^{+0.011}_{-0.008}$	$16.2985^{+0.0040}_{-0.0040}$	$0.05002^{+0.00024}_{-0.00025}$	$0.00013^{+0.00013}_{-0.00011}$	$0.536^{+0.013}_{-0.012}$
-0.001	ABC	$0.0004^{+0.0092}_{-0.0089}$	$6.0108^{+0.0099}_{-0.0098}$	$16.2973^{+0.0040}_{-0.0040}$	$0.05014^{+0.00025}_{-0.00025}$	$0.00108^{+0.00012}_{-0.00011}$	$0.521^{+0.012}_{-0.012}$

Best-fit parameters and 68.3% confidence intervals for models involving selected fixed values for the acceleration parameter $\hat{\alpha}_*^\perp$ using the full dataset corresponding to dense sampling for which $\hat{\alpha}_*^\perp$ had been adopted.

Table 9. χ^2 - and run test for models with fixed acceleration parameters.

$\hat{\alpha}_*^\perp$ [h^{-1}]	Region	χ_{\min}^2	d.o.f.	P_{χ^2}	N	N_+	N_-	$\mathcal{E}(n_r)$	$\sigma(n_r)$	n_r^{obs}	δ	P_r
0.01	ABC	439.0	147	4.3×10^{-70}	153	78	75	77.47	6.16	39	6.24	2.1×10^{-10}
0.003	ABC	191.6	147	7.8×10^{-3}	153	77	76	77.49	6.16	75	0.41	0.34
0.001	ABC	164.5	147	0.15	153	73	80	77.33	6.15	83	-0.92	0.82
-0.01	ABC	496.7	147	3.3×10^{-92}	153	78	75	77.47	6.16	44	5.43	2.8×10^{-8}
-0.003	ABC	185.2	147	0.018	153	75	78	77.47	6.16	70	1.21	0.11
-0.001	ABC	161.9	147	0.19	153	77	76	77.50	6.16	73	0.73	0.23

On the full set of $N = 153$ data points, the χ^2 -minimization yielded χ_{\min}^2 with $P_{\chi^2} = P(\chi^2 \geq \chi_{\min}^2)$ and the run test revealed N_+ positive and N_- negative residuals, for which $\mathcal{E}(n_r)$ runs with a standard deviation $\sigma(n_r)$ are expected, whereas n_r^{obs} have been found, yielding $\delta = [\mathcal{E}(n_r) - n_r^{\text{obs}}]/\sigma(n_r)$, corresponding to a probability $P_r = P(n_r \leq n_r^{\text{obs}})$.

from both Table 8 and Table 9 and the comparison with the models parameters and their uncertainties for vanishing acceleration as listed in Table 3, the effects of acceleration become negligible for $\hat{\alpha}_*^\perp = \pm 0.001 \text{ h}^{-1}$.

7.3 Influence on limb-darkening measurement

In general, acceleration can be assessed by including $\hat{\alpha}_*^\perp$ as additional free parameter in models of the lightcurve. If it cannot be accurately determined, degeneracies with other model parameters can lead to an increase of their uncertainties. Although variations of the amount of limb darkening and of acceleration provide different signatures over the full course of the caustic passage as previously shown, similar effects in local regions of the lightcurve can arise so that with a partial sampling their origin cannot be resolved and the measurement of the limb-darkening coefficient is blurred by the possible presence of significant acceleration.

The uncertainties on best-fit model parameters including a free acceleration parameter $\hat{\alpha}_*^\perp$ based on the simulated dataset for several selected regions of the lightcurve shown in Table 10 and the results of a χ^2 test shown in Table 11 demonstrate that acceleration affects models for which the caustic passage duration cannot be determined with sufficient accuracy, while otherwise a precise measurement of the acceleration leaves both the other model parameters and their uncertainties practically unchanged and the uncertainty of the measurement of the linear limb-darkening coefficient does not suffer from acceleration effects as a comparison with models for the same regions that neglect acceleration effects listed in Table 3 shows.

Even with the adopted dense sampling of the outside region A alone, for which the acceleration parameter is compatible with

values of the order of $|\hat{\alpha}_*^\perp| \sim 0.1 \text{ h}^{-1}$, a meaningful measurement of Γ cannot be obtained and large parameter degeneracies arise if acceleration is considered to be a free parameter. In contrast, if data in the outside region are combined with data from at least one of the other regions, the amount of acceleration is accurately determined and therefore does not influence the uncertainties on other parameters already for the more sparse sampling. Without a dense sampling of the outside region, the remaining parts of the lightcurve need to be densely sampled in order to yield a meaningful measurement of the linear limb-darkening coefficient, where its uncertainty is increased by a factor of two compared to the assumption of vanishing acceleration.

Data taken over all regions allows to assess the acceleration parameter accurately, down to $|\hat{\alpha}_*^\perp| \lesssim 10^{-3} \text{ h}^{-1}$ for the sparse sampling and even down to $|\hat{\alpha}_*^\perp| \lesssim 6 \times 10^{-4} \text{ h}^{-1}$ for the dense sampling, which is sufficient for acceleration effects on the lightcurve and the determination of the other parameters and their uncertainties to become negligible.

In any case, parameter degeneracies involving acceleration can be limited by adopting an upper limit on $|\hat{\alpha}_*^\perp|$ resulting from an assessment of the dynamics of the binary lens and the Earth's motion at the time of observations.

8 SUMMARY AND RECOMMENDATIONS ON OBSERVING STRATEGY

As laid out by Schneider & Weiß (1987), the differential magnification across the face of a source during its passage over a caustic created by an intervening gravitational lens can reveal its radial brightness profile through frequent accurate photometric observations. Galactic microlensing surveys such as OGLE-III are capable

Table 10. Best-fit model parameters including acceleration and their uncertainties for the simulated data in selected regions.

Region	t_f^* [h]	t_\star^\perp [h]	m_f^*	g_f^*	$-\hat{\omega}_f^*$ [h ⁻¹]	$\hat{\alpha}_\star^\perp$ [h ⁻¹]	Γ
ABC	$0.0000^{+0.0091}_{-0.0089}$	$6.003^{+0.011}_{-0.011}$	$16.2968^{+0.0040}_{-0.0040}$	$0.05019^{+0.00025}_{-0.00025}$	$0.00100^{+0.00013}_{-0.00012}$	$-0.00020^{+0.00057}_{-0.00057}$	$0.513^{+0.013}_{-0.013}$
abc	$-0.001^{+0.023}_{-0.022}$	$6.014^{+0.023}_{-0.026}$	$16.292^{+0.013}_{-0.013}$	$0.05012^{+0.00085}_{-0.00085}$	$0.00140^{+0.00046}_{-0.00042}$	$-0.0009^{+0.0012}_{-0.0011}$	$0.526^{+0.031}_{-0.031}$
ab	$0.06^{+0.11}_{-0.16}$	$5.96^{+0.13}_{-0.13}$	$16.41^{+0.17}_{-0.22}$	$0.0426^{+0.027}_{-0.006}$	$0.011^{+0.010}_{-0.018}$	$0.0011^{+0.0079}_{-0.0056}$	$0.44^{+0.10}_{-0.14}$
ac	$-0.017^{+0.028}_{-0.026}$	$6.002^{+0.025}_{-0.027}$	$16.291^{+0.013}_{-0.013}$	$0.05026^{+0.00088}_{-0.00088}$	$0.00133^{+0.00047}_{-0.00043}$	$-0.0008^{+0.0015}_{-0.0014}$	$0.494^{+0.043}_{-0.042}$
BC	$0.0^{+0.5}_{-1.2}$	$6.00^{+0.26}_{-0.60}$	$16.4^{+2.4}_{-1.4}$	$0.04^{+0.14}_{-0.04}$	$0.0008^{+0.0093}_{-0.0013}$	$-0.0017^{+0.0060}_{-0.0080}$	$0.506^{+0.064}_{-0.069}$
A	$-0.026^{+0.026}_{-0.021}$	$4.5^{+4.9}_{-0.9}$	$16.3008^{+0.0070}_{-0.0070}$	$0.066^{+0.017}_{-0.035}$	$0.00173^{+0.00092}_{-0.00095}$	$0.073^{+0.014}_{-0.084}$	$0.466^{+0.044}_{-0.043}$

The true parameters are $t_f^* = 0$, $t_\star^\perp = 6$ h, $m_f^* = 16.3$, $g_f^* = 0.05$ ($\hat{t} = 1$ h), $\hat{\omega}_f^* = -0.001$ h⁻¹, $\hat{\alpha}_\star^\perp = 0$ and $\Gamma = 0.5$. The quoted uncertainties refer to intervals enclosing a probability of 68.3 %.

Table 11. χ^2 test on models including acceleration for simulated data in selected regions and corresponding χ^2 excess of true parameters.

Region	χ_{\min}^2	d.o.f.	P_{χ^2}	$\Delta\chi_{\text{true}}^2$
ABC	160.0	146	0.20	5.6
abc	11.4	20	0.93	4.8
ab	8.4	12	0.75	5.1
ac	5.3	12	0.95	3.1
BC	111.8	96	0.13	2.3
A	43.8	43	0.44	7.7

The probability $P_{\chi^2} = P(\chi^2 \geq \chi_{\min}^2)$ provides a measure of the goodness-of-fit, while $\Delta\chi_{\text{true}}^2 = \chi^2(\mathbf{p}_{\text{true}}) - \chi^2(\mathbf{p}_{\min})$ gives the excess in χ^2 of the true parameter set \mathbf{p}_{true} over the best-fit parameter set \mathbf{p}_{\min} .

of providing ~ 10 such passages of stars in the Galactic bulge per year from which a measurement of the stellar brightness profile can be obtained, which reflects the variation of temperature with distance from the center providing a powerful technique for probing stellar atmosphere models.

Contrary to caustic entries, the corresponding exits are predictable from data obtained during the characteristic rise in magnification to a peak (Albrow et al. 1999b; Jaroszyński & Mao 2001), which allows to schedule frequent observations before the caustic passage begins.

While the caustic passages are likely to last from a few hours to a few days, photometric measurements with 1m-class telescopes with an uncertainty of less than 1.5 % with sampling intervals of a few minutes can be obtained for stars brighter than ~ 17 th magnitude as currently being carried out by the PLANET collaboration (Dominik et al. 2002), offering the possibility to collect a few hundred data points during the course of the passage.

In the vicinity of the caustic passage, the lightcurve can be described by means of a characteristic profile function $G_f^*(\eta; \xi)$, which depends solely on the dimensionless normalized stellar brightness profile $\xi(\rho)$ as function of the fractional radius ρ and the caustic passage phase η . $G_f^*(\eta; \xi)$ can be seen as the response delivered by the caustic to the specific form of the brightness profile. The weight of the contribution of the brightness at a specific fractional radius ρ to the caustic profile function $G_f^*(\eta; \xi)$ is given by a function $\mathcal{T}(\eta, \rho)$, which measures the sensitivity of the lightcurve at the point of time that corresponds to the caustic passage phase η to a local variation of the stellar brightness profile at fractional radius ρ . An inspection of $\mathcal{T}(\eta, \rho)$ shows that the caustic passage provides a one-dimensional scan of the brightness profile where each

fractional radius is most efficiently probed as it touches the caustic, which happens twice during the course of the caustic passage, so that the majority of information about outer radii is provided at the beginning and the end of the caustic passage, while inner regions of the source reveal their identity close to times when the source center passes. However, the integrated sensitivity over the full duration of the caustic passage increases with fractional radius.

In general, the extraction of the stellar brightness profile $\xi(\rho)$ from the observed lightcurve $m_{\text{fold}}(t)$ involves the determination of 5 model parameters (t_f^* , t_\star^\perp , m_f^* , g_f^* , $\hat{\omega}_f^*$), which relate $m_{\text{fold}}(t)$ and the caustic profile function $G_f^*(\eta; \xi)$, as well as the solution of the integral equation, which relates $G_f^*(\eta; \xi)$ and $\xi(\rho)$ by means of the caustic sensitivity function $\mathcal{T}(\eta, \rho)$.

The variation of coefficients characterizing a parametrized stellar brightness profile causes variations in the observed lightcurve through variations of the brightness profile at all fractional radii. The sensitivity of the lightcurve to variations in such a coefficient Γ therefore depends both on the properties of $\mathcal{T}(\eta, \rho)$ and $\partial\xi(\rho; \Gamma)/\partial\Gamma$. For linear limb darkening, this sensitivity is largest near the beginning of a caustic exit, followed by the surroundings of its end, whereas the smaller integrated sensitivity over the caustic passage for smaller fractional radii and the fact that $\partial\xi(\rho; \Gamma)/\partial\Gamma$ shows little variation with ρ for the inner parts of the source imply a small sensitivity while these pass the caustic. However, the identification of the end of the caustic exit with the characteristic feature of a jump discontinuity in its slope allows a direct measurement of the corresponding point of time t_f^* and magnitude m_f^* , while data points just after the end of the caustic exit can be used to measure the parameter $\hat{\omega}_f^*$ directly, which characterizes the variation of magnification due to non-critical images of the source. For this reason, sampling of the surroundings of the end of the caustic exit is more valuable than of its beginning. Monitoring of both of these regions provides direct measurements of the caustic passage half-duration t_\star^\perp and the caustic rise parameter g_f^* .

Unless a precision measurement on the linear limb-darkening coefficient Γ is desired, a sampling interval at the limit of the capabilities of the monitoring campaign is not required. For a caustic passage lasting 12 h, a sampling interval of ~ 30 min (corresponding to ~ 25 – 30 data points) is sufficient to provide Γ with an uncertainty of less than ~ 8 %, while a dense sampling corresponding to an interval of ~ 6 min (with ~ 150 data points) would reduce the uncertainty to less than ~ 3 %. This offers the possibility for measuring limb-darkening coefficients in several broadband filters with the same telescope on the same microlensing event or to monitor other microlensing events during the same night (e.g. to look for anomalies caused by planets around the lens stars).

Since coverage of the surroundings of the end of a caustic exit is most effective in providing an accurate measurement of the linear limb-darkening coefficient, it should be the goal of any observation strategy to try to obtain data in this region, where the sampling rate should be chosen with regard to the desired accuracy of the measurement and the number of broadband filters. Moderate sampling over other regions of the light curve is more valuable than an increased sampling over the end of the caustic exit, where a very dense sampling over these other regions however does not provide much additional information but can be used to compensate for a missing coverage of some parts of the caustic passage.

The adoption of an inappropriate stellar brightness profile or the neglect of acceleration effects, which include contributions due to the revolution of the Earth around the Sun or the orbital motion within the binary lens or a possible binary source, leads to well-distinguishable characteristic systematics in the model residuals. Although acceleration is unlikely to cause significant effects on the lightcurve for most events, if used as a free model parameter, however, it blurs the measurement of the stellar brightness profile if the duration of the caustic passage cannot be determined with sufficient accuracy, which is the case if only the surroundings of the end of the caustic exit are sampled. Nevertheless, the related degeneracy can be limited by applying a reasonable upper limit to the absolute amount of acceleration resulting from an assessment of the dynamical properties of the binary lens and the Earth's motion at the time of observation.

ACKNOWLEDGMENTS

This work has been made possible by postdoctoral support on the PPARC rolling grant PPA/G/O/2001/00475.

REFERENCES

- Afonso C., et al., 2000, *ApJ*, 532, 340
 Albrow M. D., et al., 1998, *ApJ*, 509, 687
 Albrow M. D., et al., 1999a, *ApJ*, 522, 1011
 Albrow M. D., et al., 1999b, *ApJ*, 522, 1022
 Albrow M. D., et al., 2000, *ApJ*, 534, 894
 Albrow M. D., et al., 2001, *ApJ*, 549, 759
 An J. H., et al., 2002, *ApJ*, 572, 521
 Ansari R., 1994, Une méthode de reconstruction photométrique pour l'expérience EROS, preprint LAL 94-10
 Dominik M., 1996, PhD thesis, Universität Dortmund
 Dominik M., 1998, *A&A*, 329, 361
 Dominik M., 1999, *A&A*, 349, 108
 Dominik M., 2003, Theory and practice of microlensing light-curves around fold singularities, astro-ph/0309581
 Dominik M., et al., 2002, *P&SS*, 50, 299
 Erdl H., Schneider P., 1993, *A&A*, 268, 453
 Fields D. L., et al., 2003, *ApJ*, 569, 1305
 Gaudi B. S., Gould A., 1999, *ApJ*, 513, 619
 Heyrovský D., 2003, *ApJ*, 594, 464
 Jaroszyński M., Mao S., 2001, *MNRAS*, 325, 1546
 Rhie S. H., Bennett D. P., 1999, Line Caustic Microlensing and Limb Darkening, astro-ph/9912050
 Schneider P., Wagoner R. V., 1987, *ApJ*, 314, 154
 Schneider P., Weiß A., 1987, *A&A*, 171, 49
 Smith M. C., Mao S., Paczyński B., 2003, *MNRAS*, 339, 925
 Tsapras Y., Horne K., Kane S., Carson R., 2003, *MNRAS*, 343, 1131
 Udalski A., et al., 1994, *Acta Astronomica*, 44, 165
 Yoo S. H., et al., 2003, OGLE-2003-BLG-262: Finite-Source Effects from a Point-Mass Lens, astro-ph/0309302